Optimal dynamic induction control of a pair of inline wind turbines

Ali Emre Yılmaz, and Johan Meyers

Citation: Physics of Fluids **30**, 085106 (2018); doi: 10.1063/1.5038600
View online: https://doi.org/10.1063/1.5038600
View Table of Contents: http://aip.scitation.org/toc/phf/30/8
Published by the American Institute of Physics

Optimal dynamic induction control of a pair of inline wind turbines

Ali Emre Yılmaz[a] and Johan Meyers[b]
Department of Mechanical Engineering, KU Leuven, Celestijnenlaan 300–Bus 2421, B3001 Leuven, Belgium

(Received 4 May 2018; accepted 1 August 2018; published online 21 August 2018)

We study dynamic induction control for mitigating the wake losses of a pair of inline wind turbines. In order to explore control strategies that account for unsteady interactions with the flow, we employ optimal control and adjoint-based optimization in combination with large-eddy simulations. The turbines are represented with an actuator line model. We consider a simple uniform inflow case with two NREL 5 MW turbines spaced 5 diameters apart and find that optimal control leads to 25% gains compared to standard Maximum-Power-Point Tracking (MPPT). It is further found that only the control dynamics of the first turbine are changed, improving wake mixing, while the second turbine controller remains close to the MPPT control. We further synthesize the optimal generator torque and blade pitch controls of the first turbine into a signal that can be periodically used as an open-loop controller, with a Strouhal number of 0.38, while realizing the same gains as the original optimal control signal. Further analysis of the improved wake mixing resulting from the open-loop signal reveals periodic shedding of a three-vortex ring system, which interacts and merges downstream of the first turbine, increasing entrainment of high-speed momentum into the wake. The sensitivity of the open-loop signal to inlet turbulence levels and turbine spacing is also investigated. At low to medium turbulence levels, the control remains effective, while at higher levels, the coherence of the vortex rings degrades too fast for them to remain effective. *Published by AIP Publishing.*
https://doi.org/10.1063/1.5038600

I. INTRODUCTION

An important challenge in wind farms is the efficiency loss induced by turbine wakes on downstream turbines. In various operational wind farms, and depending on the farm layout and the wind direction, losses as much as 60% have been reported in individual turbines compared to front-row turbines.[1–3] These findings have also been supported by several Large-Eddy Simulation (LES) studies.[4–7] The problem is inherent to the existence of turbine wakes and cannot be completely avoided unless there is more than 15–20 rotor diameters of distance between the wind turbines so that wakes can completely recover due to turbulent mixing. However, in large wind farms, this is economically not interesting, as the spacing between turbines is dictated by other aspects such as site development cost, cabling costs, etc.[6,8] Active control strategies that take wake interaction into account may play a key role in mitigating power losses due to turbine wakes, thus decreasing the levelized cost of energy in wind farms.

At below-rated wind speeds, the conventional approach in wind-turbine control (also standardly used for turbines in a farm) is based on maintaining the peak aerodynamic efficiency for each turbine individually. At above-rated wind speeds, turbines operate at rated power and adapt their aerodynamic efficiency by blade pitch to maintain a constant rotational speed. In wind farms, the latter regime is not amenable for further power optimization, as turbines are already at their maximum output, but in the former regime, it may be beneficial to take wake interaction into account and coordinate the control of the turbines in the farm.

In the past, numerous studies have attempted to develop coordinated control strategies for wind farms—most of them have focused on static approaches. One of the earliest studies in this direction was performed by Steinbuch *et al.*[9] They focussed on statically downrating the first rows of a farm, reducing their wake strength, and increasing energy extraction in downstream turbines, with the overall aim to realize a net positive balance in energy extraction. This type of control approach is often called axial induction control. However, recent research based on high-fidelity LES, as well as wind-tunnel experiments, has revealed that static axial induction control provides minor benefits at best.[10,11] Earlier positive results are now attributed to the use of wake engineering models that were not sufficiently sophisticated to properly capture the relevant physics of wake mixing.[10] Another static approach to optimizing wind-farm power extraction is based on wake redirection using the turbine yaw angle. In contrast to static induction control, this approach has been shown to be successful both in LES and in experiments.[12–14]

The use of wind-farm control in which turbine controls interact dynamically with the turbulent background flow in the wind-farm boundary layer with the aim to increase power extraction is much less studied. First work in this direction was presented by Goit and Meyers.[15] They used optimal control based on LES to optimize the interaction between dynamic turbine induction control and a fully developed wind-farm boundary layer. Later, the approach was extended to wind farms with entrance effects,[16,17] with

[a]E-mail: aliemre.yilmaz@kuleuven.be
[b]E-mail: johan.meyers@kuleuven.be

power gains up to 20%, depending on control speed and constraints on the maximum induction.[17] Very recently, dynamic yaw control was also considered based on the same methodology.[18]

The above work on optimal dynamic induction control of wind farms[15–17] has focused on the use of LES as a control model so that the detailed turbulence physics of wake mixing and interaction with the boundary layer are accounted for when optimizing the controls. The main rationale behind these studies did not envisage the use of LES as a real-time control model (which is computationally not feasible), but rather used the approach to explore new physical mechanisms that can be used to improve wind-farm energy extraction. For instance, one of the salient features found in optimal dynamic induction control of wind farms is the excitation of vortex rings behind the first-row turbines, which increase wake mixing and downstream power output.[19] However, these findings are all based on LES using an actuator disk model (ADM) as a turbine model, controlling the disk-based thrust coefficient of each individual turbine in the LES. Given current-day computational resources, this is unavoidable when considering coordinated control of wind farms in LES. Nevertheless, the use of an ADM simplifies the representation of turbulence in the near wake. Moreover, even though disk-based thrust coefficients in ADM are indirectly related to generator torque and blade-pitch set points, it remains a simplified representation that does not include the full degrees of freedom nor the limitations of real turbine control. Therefore, in the current work, we focus on the use of LES-based optimal control in combination with an actuator line model (ALM). Moreover, instead of performing optimal control of an entire wind farm, we study a two-turbine setup with uniform inflow conditions so that the simulation resolution can be sufficiently refined to warrant the use of an ALM. Similar to earlier results using an ADM,[19] we find that optimal control with an ALM leads to the excitation of vortex rings in the wake of the leading turbine, resulting in better wake mixing. However, the finer resolution and improved model highlight different features related to the vortex dynamics and pairing. Moreover, based on our results, we identify simple open-loop control signals that reproduce these features and can be straightforwardly tracked by means of a conventional control.

The paper is organized as follows. Section II introduces the LES-based optimal control methodology. Subsequently, the computational setup and scope of the current study are presented in Sec. III. Results are discussed in Sec. IV, and conclusions are presented in Sec. V.

II. METHODOLOGY

First, in Sec. II A, we present the receding-horizon optimal-control framework that we use in the current work. Next, in Sec. II B, the forward simulation system is presented, corresponding to large-eddy simulations of a set of wind turbines using ALM. The optimal control problem is subsequently formulated in Sec. II C, including the formulation of the adjoint equations. Finally, in Sec. II D, some implementation details related to the adjoint time integration are discussed.

A. Receding horizon optimal control framework

Similar to earlier work on optimal control in wind-farm LES,[15–17] we use a receding-horizon framework to optimize the interactions between the wind-turbine controls and the turbulent flow. The concept is illustrated in Fig. 1.

First of all, we define an optimal control time horizon T. Next, at simulation time $t = 0$, we optimize the turbine controls (generator torques and blade pitch angles) over the time horizon T given the full interaction with the turbulent flow during this time horizon. This requires the solution of a large optimization problem, with multiple large-eddy simulations and adjoint large-eddy simulations as further described in Sec. II C. On average, this optimization requires $N_s = 60$ simulations (LES or adjoint LES)—see Sec. III for details of the computational setup.

Once this optimization problem is solved, the optimal controls are used to advance the system in time, but only for a time window $T_A < T$, so that optimization finite-horizon-effects are truncated from the controls. (Finite-horizon-effects are explained in Appendix C.) We now arrive at $t = T_A$ and start a new optimization problem over the time window $[T_A, T_A + T]$, and so on. Thus, overall, this receding horizon approach is $N_s * T/T_A$ times more expensive than a standard large-eddy simulation with wind turbines.

It is best to keep the length of the optimization time horizon T as long as possible so that the wind turbines have plenty of time to interact. However, in practice, T is limited by the accuracy of the adjoint-based gradient, which diverges for too long time horizons (see, e.g., Refs. 20–22 for a theoretical background). Therefore, we select T sufficiently long for our purposes (see Appendix C for an evaluation of our gradient accuracy). Next to this, the ratio T_A/T should be selected as low as possible to guarantee a smooth transition between optimal control signals of successive optimization windows. Nevertheless, the total computational cost scales with T/T_A. In earlier optimal-control studies in turbulence resolving simulations, $T_A = T$ (e.g., Ref. 23) and $T_A = T/2$ (e.g., Refs. 23 and 15) have been typically used. Recently, in Ref. 17, it was shown that $T_A = T/4$ results in a much smoother transition between the control signals compared to $T_A = T/2$. In view of these, in the current study, we use $T_A = T/3$ as a trade-off between signal smoothness and computational cost.

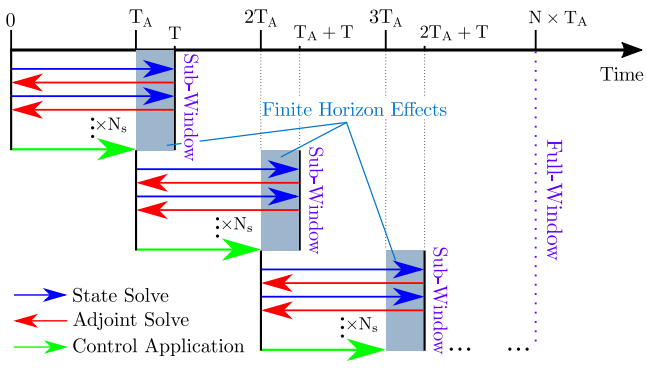

FIG. 1. Receding horizon control.

B. Forward system

The forward LES simulations are performed in SP-Wind,[24] an in-house pseudo-spectral Navier-Stokes (NS) solver. The governing equations are based on the filtered NS equations for incompressible flow, i.e.,

$$\nabla \cdot \widetilde{\boldsymbol{u}} = 0, \tag{1a}$$

$$\frac{\partial \widetilde{\boldsymbol{u}}}{\partial t} + \widetilde{\boldsymbol{u}} \cdot \nabla \widetilde{\boldsymbol{u}} = -\frac{1}{\rho}\nabla \widetilde{p} - \nabla \cdot \boldsymbol{\tau} + \boldsymbol{f}, \tag{1b}$$

where $\widetilde{\boldsymbol{u}} = [\widetilde{u}_1, \widetilde{u}_2, \widetilde{u}_3]$ is the velocity, $\widetilde{p}$ is the pressure, $\boldsymbol{\tau}$ is the subgrid scale stress, and $\boldsymbol{f}$ the wind turbine forces that are modeled using an ALM model (see below). Similar to earlier work on optimal control of wind farms, we use a standard Smagorinsky model to model the subgrid-scale stresses so that

$$\boldsymbol{\tau} = -2(C_s\Delta)^2(2\boldsymbol{S} : \boldsymbol{S})^{1/2}\boldsymbol{S}, \tag{2}$$

with the rate-of-strain tensor $\boldsymbol{S} = (\nabla\widetilde{\boldsymbol{u}} + (\nabla\widetilde{\boldsymbol{u}})^T)/2$, the grid spacing $\Delta = (\Delta_1\Delta_2\Delta_3)^{1/3}$, and where we take[25,26] $C_s = 0.14$. Further details on boundary conditions and the case setup are discussed in Sec. III, while discretization is discussed in Sec. II D.

The turbine forces $\boldsymbol{f}$ are modeled using an ALM, following Ref. 27 and many studies since then. These represent the forces by turbines on the flow, and contributions are assembled over the different turbines and blades so that $\boldsymbol{f} = \sum_{i=1}^{N_t}\sum_{j=1}^{N_b}\boldsymbol{f}^{ij}$, with $\boldsymbol{f}^{ij}$ being the force coming from blade j of turbine i and N_t and N_b being the number of turbines and blades per turbine, respectively. In our current study, $N_b = 3$, and $N_t = 2$.

In order to calculate the blade forces $\boldsymbol{f}^{ij}$, it is assumed that the blades can be represented by lifting lines. Along these lines, lift and drag forces are obtained using the local relative velocity, and using tabulated values for lift and drag coefficients. This results in blade section forces $\boldsymbol{F}^{ij}(\mu, \theta^i)$ along the blade span, with $\mu = r/R$ $(0 \le \mu \le 1)$ being a scalar that parametrizes the blade along its span (see below for expressions of $\boldsymbol{F}^{ij}$), R being the radius of the rotor, and $\theta^i(t)$ being the position angle of the turbine rotor. The concept is illustrated in Fig. 2. Note that we presume that the rotor is always perpendicular to the x_1-direction and that the blades can be parametrized with straight actuator lines. Its coordinates are given by $\boldsymbol{x}^{ij}(\theta^i, \mu) = [x_1^i,\ x_2^i + R\mu\cos(\theta^i + \Delta\theta^j),\ x_3^i + R\mu\sin(\theta^i + \Delta\theta^j)]$,

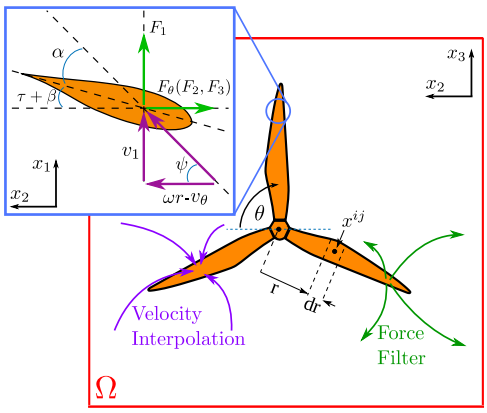

FIG. 2. Actuator line model. Outline of the main approach and relevant parameters.

with $\boldsymbol{x}^i$ being the coordinates of the hub of turbine i, R being the radius, and $\Delta\theta^j = (j-1)2\pi/N_b$ being the angle offset of blade j.

The forces $\boldsymbol{f}^{ij}$ on the flow are obtained by filtering the blade section forces using a three-dimensional Gaussian filter, leading to

$$\boldsymbol{f}^{ij}(\boldsymbol{x}, t) = -\int_0^1 G(\boldsymbol{x} - \boldsymbol{x}^{ij}(\mu))\boldsymbol{F}^{ij}(\mu, \theta^i(t))\,\mathrm{d}\mu, \tag{3}$$

where

$$G(\boldsymbol{x}) = \frac{(6/\pi)^{3/2}}{\epsilon_1\epsilon_2\epsilon_3}\exp\left(-6\left(\frac{x_1^2}{\epsilon_1^2} + \frac{x_2^2}{\epsilon_2^2} + \frac{x_3^2}{\epsilon_3^2}\right)\right) \tag{4}$$

is the Gaussian filter kernel, with ϵ_k being the directional filter widths.

The force $\boldsymbol{F}^{ij}$ per unit span and per unit density is further expressed using standard blade-element theory as[28]

$$\begin{aligned} F_1^{ij} &= q^{ij}\left(C_l\cos\psi^{ij} + C_d\sin\psi^{ij}\right)c(\mu), \\ F_2^{ij} &= -q^{ij}\left(C_l\sin\psi^{ij} - C_d\cos\psi^{ij}\right)c(\mu)\sin(\theta^i + \Delta\theta^j), \\ F_3^{ij} &= q^{ij}\left(C_l\sin\psi^{ij} - C_d\cos\psi^{ij}\right)c(\mu)\cos(\theta^i + \Delta\theta^j), \end{aligned} \tag{5}$$

where $q^{ij} = [(v_1^{ij})^2 + (\omega_i R\mu - v_\theta^{ij})^2]/2$ and v_1^{ij} and $v_\theta^{ij} = -v_2^{ij}\sin(\theta) + v_3^{ij}\cos(\theta)$ are the local axial and tangential velocity on the blade, respectively. Note that they depend on μ and $\theta^i + \Delta\theta^j$, which we have dropped from the notation for simplicity. Furthermore, $c(\mu)$ is the blade chord, $\psi^{ij} = \arctan(v_1^{ij}/(\omega_i R\mu - v_\theta^{ij}))$ is the flow angle, and C_l and C_d are the lift and drag coefficients of the blade profile along the span. They depend on the location μ and on the local angle of attack $\alpha^{ij} = \psi^{ij} - \varsigma - \beta^i$, where $\varsigma(\mu)$ is the twist angle, and $\beta^i(t)$ is the collective blade pitch angle of turbine i (which is a control parameter).

The ALM velocities $\boldsymbol{v}$ on the lifting line are obtained by interpolating the LES velocity $\widetilde{\boldsymbol{u}}$. To this end, a linear interpolation is applied, which corresponds in kernel notation to

$$\boldsymbol{v}^{ij}(\mu, \theta^i(t)) = \int H(\boldsymbol{x} - \boldsymbol{x}^{ij}(\theta^i, \mu))\widetilde{\boldsymbol{u}}(\boldsymbol{x}, t)\,\mathrm{d}\boldsymbol{x}, \tag{6}$$

with $H(\boldsymbol{x}) = \prod_{k=1}^3 H_k(x_k)$ and

$$H_k(x) = \max\left(1 - \frac{|x|}{\Delta_k}, 0\right), \tag{7}$$

where we use the LES grid spacing for Δ_k. Note that the particular choice of convolution notation we use here is for ease of derivation of the adjoint equations (see Appendix A).

Finally, the rotor position and rotor dynamics are given by

$$\frac{\mathrm{d}\boldsymbol{\theta}}{\mathrm{d}t} = \boldsymbol{\omega}(t), \tag{8}$$

$$J\frac{\mathrm{d}\boldsymbol{\omega}}{\mathrm{d}t} = \boldsymbol{T}_a(t) - \boldsymbol{T}_g(t), \tag{9}$$

with $\boldsymbol{\theta} = [\theta^1, \ldots, \theta^{N_t}]$ and $\boldsymbol{\omega} = [\omega^1, \ldots, \omega^{N_t}]$ vectors containing the rotor positions and rotational speeds of all turbines. Furthermore, J is the turbine inertia (presumed the same for

all turbines), $\boldsymbol{T}_g(t) = [T_g^1, \ldots, T_g^{N_t}]$ is a vector with all generator torques of the turbines (which are control parameters), and $\boldsymbol{T}_a = [T_a^1, \ldots, T_a^{N_t}]$ is the vector with all aerodynamical torques generated by the turbine blades. The latter follows from $T_a^i = \int_0^1 \sum_{j=1}^{N_b} T_a^{ij}\, \mathrm{d}\mu$, with

$$T_a^{ij} = q^{ij}\left(C_l \sin\psi^{ij} - C_d \cos\psi^{ij}\right) c(\mu) R\, \mu \tag{10}$$

being the blade section torques per unit span and per unit density. For the verification of the implemented ALM, the reader is referred to Ref. 52.

The above turbine model has two control inputs per turbine, which are the generator torque $T_g^i(t)$ and collective pitch angle $\beta^i(t)$. In Sec. II C, we will present the optimal control problem that we use to optimize these controls. However as a point of reference, we will also consider a standard maximum power-point tracking (MPPT) region-2 controller. It keeps the pitch angle at the optimal design setting and regulates the generator torque using[29]

$$T_g^i = K\omega_i^2, \quad \text{with } K = \frac{1}{2}\rho\pi R^5 \frac{C_p^*}{\lambda_*^3}, \tag{11}$$

where C_p^* and λ_* are the optimal design power coefficient and design tip speed ratio, respectively, which we take the same for all turbines. For the NREL-5 MW turbine used in the current study,[30] the optimal control setting in region-2 reads K = 2.17 $\times 10^6$ kg m^2 and $\beta = 0°$ based on the classical blade element momentum theory. However, when coupling the ALM with a Navier-Stokes solver, these values depend on the filter width used for the filtering of the ALM forces.[31,32] For the grid resolution and filter width used in the current study, the optimal value of K is found to be 2.02×10^6 kg m^2. Similarly, the optimal blade pitch angle is found to be $\beta = -1°$. These values are employed for the reference MPPT simulations.

C. Optimization problem and continuous adjoint equations

As discussed in Sec. II A, we employ a moving horizon optimal control framework to optimize $T_g^i(t)$ and $\beta^i(t)$ over a time horizon $[0, T]$. For the sake of compact notation, we assemble all controls in one control vector $\boldsymbol{\varphi} = [\boldsymbol{T}_g(t), \boldsymbol{\beta}(t)]$, with $\boldsymbol{T}_g(t)$ defined above and $\boldsymbol{\beta} = [\beta^1(t), \ldots, \beta^{N_t}(t)]$.

The cost functional that we use in the optimization problem corresponds to

$$\begin{aligned}\mathscr{J}(\boldsymbol{\varphi}, \boldsymbol{q}) = &\int_0^T -\boldsymbol{T}_g(t)\cdot\boldsymbol{\omega}(t)\, \mathrm{d}t \\ &+ \int_0^T \sum_{i=1}^{N_t} \Big(\gamma_1 \left[\max\left(0, \omega_i(t) - \omega^{max}\right)\right]^2 \\ &+ \gamma_2 \left[\max\left(0, \omega^{min} - \omega_i(t)\right)\right]^2\Big)\, \mathrm{d}t,\end{aligned} \tag{12}$$

where for ease of notation we assembled all state variables coming from Eqs. (1), (8), and (9) into one vector $\boldsymbol{q} = [\widetilde{\boldsymbol{u}}(\boldsymbol{x}, t), p(\boldsymbol{x}, t), \boldsymbol{\theta}(t), \boldsymbol{\omega}(t)]$. The above cost function maximizes power extraction in the farm but adds two additional penalty terms scaled with constants γ_1 and γ_2. These introduce soft constraints on the rotational speed, which are related to the state variables, and are as such difficult and expensive to add as hard constraints in the optimization problem. We employ $\omega^{max} = 12.1$ rpm in accordance with the limits on the NREL-5 MW turbine. Moreover, $\omega^{min} = 0$ to prevent the rotor from switching to fan mode. Furthermore, we use values $\gamma_1 = \gamma_2 = 10^9$ so that the penalization terms attain values on a similar order of magnitude with the produced power for slight violations of the constraints. In practice, we observe that the rotational-speed constraints are almost never violated in our optimal control results.

Given the above cost functional and the state equations presented in Sec. II B, we arrive at the following optimization problem, which we formulate directly in its reduced formulation (see, e.g., Refs. 33 and 15):

$$\begin{aligned}&\min_{\boldsymbol{\varphi}} \quad \tilde{\mathscr{J}}(\boldsymbol{\varphi}) \equiv \mathscr{J}(\boldsymbol{\varphi}, \boldsymbol{q}(\boldsymbol{\varphi})), \\ &s.t. \\ &\quad \beta_{min} \leqslant \beta^i(t) \leqslant \beta_{max} \quad \text{for } i = 1 \cdots N_t, \\ &\quad T_{min} \leqslant T_g^i \leqslant T_{max} \quad \text{for } i = 1 \cdots N_t.\end{aligned} \tag{13}$$

Here, $\boldsymbol{q}(\boldsymbol{\varphi})$ corresponds to the solution of the state equations given the controls $\boldsymbol{\varphi}$. Thus during optimization, the state equations are satisfied at every step, while we iterate on $\boldsymbol{\varphi}$ to find the optimal controls.

To solve the optimization problem (13), we use a Limited-memory Broyden–Fletcher–Goldfarb–Shanno method for Bound-constrained optimization (L-BFGS-B),[34] similar to earlier work in Ref. 17. L-BFGS-B is a gradient based quasi-Newton method, which estimates an approximation to the true Hessian of the optimization problem by using a BFGS updating scheme and employs a gradient projection technique to handle simple box-constraints.[34] The method is gradient based and thus requires the gradient of the cost functional $\nabla\tilde{\mathscr{J}} = [\nabla\tilde{\mathscr{J}}_\beta, \nabla\tilde{\mathscr{J}}_T]$ (with $\nabla\tilde{\mathscr{J}}_\beta$ and $\nabla\tilde{\mathscr{J}}_T$ being the gradient of the cost functional toward the controls $\boldsymbol{\beta}$, and $\boldsymbol{T}_g$, respectively). Before using the gradient in the L-BFGS-B method, we first apply a preconditioning. We observe that $\nabla\tilde{\mathscr{J}}_\beta$ is on average eight orders of magnitude larger than $\nabla\tilde{\mathscr{J}}_T$, and therefore, we scale $\nabla\tilde{\mathscr{J}}_\beta$ by a factor of 10^{-8}. Note that such a scaling would not be necessary in an exact Newton method, but we found it to be necessary here as the BFGS method estimates the Hessian based on a limited history of past gradients only, and without this scaling, optimal control results would not include any generator torque action within the limited number of iterations that we can afford in the optimization method.

The gradient of the cost function $\nabla\tilde{\mathscr{J}} = [\nabla\tilde{\mathscr{J}}_\beta, \nabla\tilde{\mathscr{J}}_T]$ is obtained using an adjoint method. This allows the calculation of the gradient at the cost of one additional set of partial differential equations (the adjoint or backward system) with a similar computation cost as the forward system. Detailed derivations are provided in Appendix A. We find the gradient as

$$\nabla\tilde{\mathscr{J}}_\beta = \sum_j \mathbf{1}_i \int_0^1 \frac{\mathrm{d}\boldsymbol{F}^{ij}}{\mathrm{d}\beta^i} \cdot \left(\int_\Omega G(\boldsymbol{x} - \boldsymbol{x}^{ij}(\mu))\boldsymbol{\xi}\, \mathrm{d}\boldsymbol{x}\right) \mathrm{d}\mu - \frac{1}{J}\frac{\mathrm{d}\boldsymbol{T}_a}{\mathrm{d}\boldsymbol{\beta}}\boldsymbol{\chi}, \tag{14}$$

$$\nabla\tilde{\mathscr{J}}_T = -\boldsymbol{\omega} + \boldsymbol{\chi}/J. \tag{15}$$

The Jacobians $\mathrm{d}\boldsymbol{F}^{ij}/\mathrm{d}\beta^i$ and $\mathrm{d}\boldsymbol{T}_a/\mathrm{d}\boldsymbol{\beta}$ are further elaborated in Appendix A. Furthermore, $\boldsymbol{\xi}$ and χ follow from the solution of the adjoint equations.

For the derivation of the adjoint equations, we use a continuous approach. Detailed derivations of the equations are provided in Appendix A, leading to

$$\nabla \cdot \boldsymbol{\xi} = 0, \tag{16}$$

$$-\frac{\partial \boldsymbol{\xi}}{\partial t} - \widetilde{\boldsymbol{u}} \cdot \nabla \boldsymbol{\xi} + (\nabla \widetilde{\boldsymbol{u}})^T \boldsymbol{\xi} - \frac{1}{\rho}\nabla \pi + \nabla \cdot \boldsymbol{\tau}^* + \boldsymbol{f}^* = 0, \tag{17}$$

$$-\frac{\mathrm{d}\chi}{\mathrm{d}t} - (\mathbb{T} + \Upsilon) - \frac{1}{J}\frac{\mathrm{d}\boldsymbol{T}_a}{\mathrm{d}\boldsymbol{\omega}}\chi + \sum_j \mathbf{1}_i \int_0^1 \frac{\mathrm{d}\boldsymbol{F}^{ij}}{\mathrm{d}\omega^i} \cdot \left(\int_\Omega G(\boldsymbol{x} - \boldsymbol{x}^{ij}(\mu))\boldsymbol{\xi}\, \mathrm{d}\boldsymbol{x} \right) \mathrm{d}\mu = 0, \tag{18}$$

$$-\frac{\mathrm{d}\Upsilon}{\mathrm{d}t} - \frac{1}{J}\frac{\mathrm{d}\boldsymbol{T}_a}{\mathrm{d}\boldsymbol{\theta}}\chi + \sum_{i,j} \int_0^1 \frac{\mathrm{d}\boldsymbol{F}^{ij}}{\mathrm{d}\theta^i} \cdot \left(\int_\Omega G(\boldsymbol{x} - \boldsymbol{x}^{ij}(\mu))\boldsymbol{\xi}\, \mathrm{d}\boldsymbol{x} \right) \mathrm{d}\mu + \sum_{i,j} \int_0^1 \boldsymbol{F}^{ij} \cdot \left(\int_\Omega \frac{\mathrm{d}G(\boldsymbol{x} - \boldsymbol{x}^{ij}(\mu))}{\mathrm{d}\theta^i}\boldsymbol{\xi}\, \mathrm{d}\boldsymbol{x} \right) \mathrm{d}\mu = 0, \tag{19}$$

where $\mathbb{T} = \boldsymbol{T}_g - 2\gamma_1 \max[0, \boldsymbol{\omega} - \omega^{max}] + 2\gamma_2 \max[0, \omega^{min} - \boldsymbol{\omega}]$. These equations need to be integrated backward in time, with terminal conditions $\boldsymbol{\xi}(T) = 0$, $\chi(T) = 0$, and $\Upsilon(T) = 0$. Furthermore, $\boldsymbol{\tau}^*$ are the adjoint subgrid-scale stresses (see Ref. 15 for details), and the adjoint ALM forces are given by

$$\boldsymbol{f}^* = \sum_{i,j} \int_0^1 H(\boldsymbol{x} - \boldsymbol{x}^{ij}) \left\{ \left(\frac{\mathrm{d}\boldsymbol{F}^{ij}}{\mathrm{d}\boldsymbol{v}^{ij}} \right)^T \cdot \left[\int_\Omega G(\boldsymbol{x} - \boldsymbol{x}^{ij})\boldsymbol{\xi}\, \mathrm{d}\boldsymbol{x} \right] - \frac{1}{J}\frac{\mathrm{d}T_a^{ij}}{\mathrm{d}\boldsymbol{v}^{ij}}\chi_i \right\} \mathrm{d}\mu. \tag{20}$$

Further details, including expressions for the Jacobians $\mathrm{d}\boldsymbol{T}_a/\mathrm{d}\boldsymbol{\omega}$, $\mathrm{d}\boldsymbol{F}^{ij}/\mathrm{d}\omega^i$, etc., are provided in Appendix A.

D. Discretization and aspects of adjoint time integration

Both the forward and adjoint equations are solved using SP-Wind, which is an in-house large-eddy simulation and optimization code developed at KU Leuven over the last decade.[15,17,35,36] The Navier–Stokes equations are discretized using a pseudo-spectral Fourier method in horizontal planes,[37] and a fourth-order energy conserving finite-difference method is used in the vertical direction.[38] Dealiasing is performed using the 3/2 rule.[37] The Poisson equation is solved using a direct method, and time integration is performed with a fourth-order four-stage Runge-Kutta method. In the axial flow direction, non-periodic boundary conditions are imposed using a fringe region method (see Ref. 39 for implementation details).

The adjoint equations are solved using the same discretization techniques.[15,17,36] During the adjoint simulation, the solution of the forward equations around which adjoint sensitivities are evaluated is required [see Eqs. (17)–(20)]. In earlier studies,[15,17,36] the forward velocity field was stored only once every time step and kept constant over the four backward Runge–Kutta stages. This reduces the required amount of disk storage by a factor of four but leads to a first-order time error between the forward and backward sensitivity. This has never led to gradient accuracy issues in earlier studies (see, e.g., Refs. 36 and 40). However with the introduction of an ALM, and the additional rotation and position equations of the turbine rotor, we found that errors introduced in this way grow unacceptably large, or adjoint simulations diverge. Therefore, in the current study, we use a discrete-adjoint Runge–Kutta time integration instead, of which the formulations can be found in Appendix B.

Overall, for the optimal control case considered in the current study (i.e., with T = 199.5 s, and using uniform non-turbulent inflow conditions, see Sec. III A for further details), we verified that the error between our adjoint gradient and a simple finite-difference evaluation of the gradient (for a few sensitivities only) remains below 10% (further details are provided in Appendix C). Nevertheless, accuracy of the gradient remains an issue when combining optimal control with a turbulent inflow, requiring further algorithm developments and research in future work. In the current paper, we restrict our optimal control simulation to one non-turbulent inflow case (also in view of large computational cost) and use results to synthesize simple open-loop control signals that are subsequently also tested for different turbulent inflow conditions.

III. COMPUTATIONAL SETUP

The optimal control study and all additional simulations in the current work are considering two inline wind turbine rotors placed in a rectangular domain as shown in Fig. 3. The domain size is $14 \times 6 \times 6$ in terms of rotor diameters. The rotor model used is NREL-5 MW,[30] with a diameter of 126 m. First, in Sec. III A, details of the optimal-control case are defined. Next in Sec. III B, additional simulation cases are defined, which are later used for testing of optimal-control signals.

A. Optimal-control case setup

In the current manuscript, we consider one optimal control case that focuses on the coordinated control of two turbines with a 5D stream-wise separation. The rotors are represented using an ALM (see Sec. II B).

The simulations are performed using two inline wind turbine rotors placed in a rectangular domain as shown in Fig. 3. The rotor model used is NREL-5 MW,[30] with a diameter of 126 m. Each blade of the rotors is represented by 50 actuator line points. The domain is discretized by an equidistant Cartesian mesh with $384 \times 192 \times 384$ grid points. This leads to approximately 31 LES grid points along the rotor diameter, which is a moderately fine discretization resolution for ALM simulations.[44] The width of the force filter [i.e., ϵ_1, ϵ_2, ϵ_3 in Eq. (4)] is 2.5 times the cell size in the corresponding direction. For the time integration, we use a time step of 0.07 s, which corresponds to a Courant–Friedrichs–Lewy number of approximately 0.12.

The upstream rotor is placed three diameters downstream of the inflow boundary in the axial flow direction. In the other directions, both rotors are placed in the center of the domain. At the inlet, a uniform inflow is imposed with a velocity of 8 m/s,

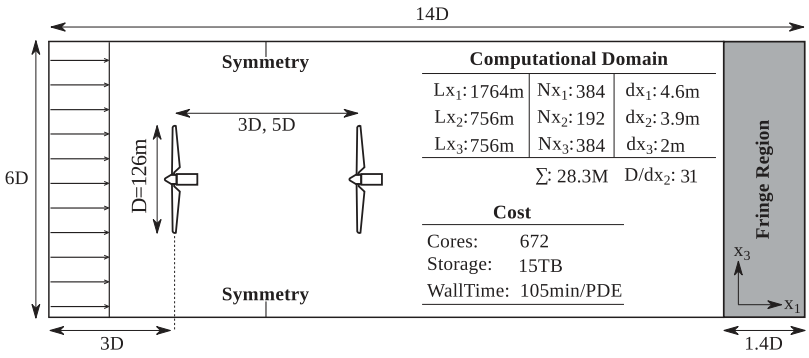

FIG. 3. Simulation setup for the optimal control case. [In the spanwise direction (x_2), the boundary conditions are periodic.]

which is well within the region-2 operation of the NREL-5 MW turbine. The inlet conditions are implemented using a classical fringe-region technique in our pseudo-spectral method.[45] In the spanwise direction, periodic boundary conditions are employed, while in the vertical direction, symmetry conditions are used. Before starting the optimal control, both rotors are operated by the MPPT controller for roughly two domain flow-through times so that the turbine wakes are fully developed. After this, we start the optimal control, which we indicate with time $t = 0$.

In our receding horizon control, we use a time horizon $T = 199.5$ s, which roughly corresponds to four to five rotor-to-rotor advection times. We further employ $T_A = T/3 = 66.5$ s (see Sec. II A) and perform in total five consecutive optimal-control time windows so that we arrive at a total optimal control time of 332.5 s, which roughly corresponds to 1.5 domain through-flow times ($\approx 21\ D/U_\infty$).

In the first iteration of our first optimization window, we initialize our controls $\boldsymbol{\varphi}$ in the L-BFGS-B algorithm by the controls that we obtain by first simulating this time window using the MPPT controller. In subsequent optimization windows (two to five), we use the optimal controls obtained from the previous window. However, instead of using the full signal $[0, T]$, we repeat the first part $[0, T_A]$ three times, as we found that it provides us with a better starting point.

During optimization, we do not formally converge the controls, but rather terminate after the control updates start to stagnate. This roughly corresponds to 25-30 L-BFGS-B iterations and 55-65 PDE simulations (forward or adjoint) per optimization window. In Fig. 4, the convergence history is shown for the five optimization windows. During forward simulations, the forward solution is stored to disk for use in subsequent adjoint simulations, requiring 15TB of disk storage. Forward and adjoint simulations are performed on 672 cores (24 nodes of Intel Broadwell, E5-2680v4), interconnected with EDR Infiniband. The forward simulation of one time window T takes approximately 105 min of wall time, with an adjoint simulation taking roughly the same. In total, the full optimal-control study over the five time horizons took 45 days of simulations.

B. Additional simulation cases

In Sec. IV, we synthesize the optimal control results obtained using the case setup described above into simple periodic control signals that can be straightforwardly applied to a wind turbine without the need for feedback or model-predictive control. We test these signals in an additional set of simulation cases.

A first set of simulation cases simply repeats the uniform inflow setup described above, and a second set of cases uses a turbulent inflow on the same grid. To this end, Mann turbulence[46] is added to the uniform inflow, generated using the TuGen library.[47] Three different turbulence intensities are considered (1%, 5%, and 10%), as well as four different integral length scales (8 m, 15 m, 30 m, and 63 m). Moreover,

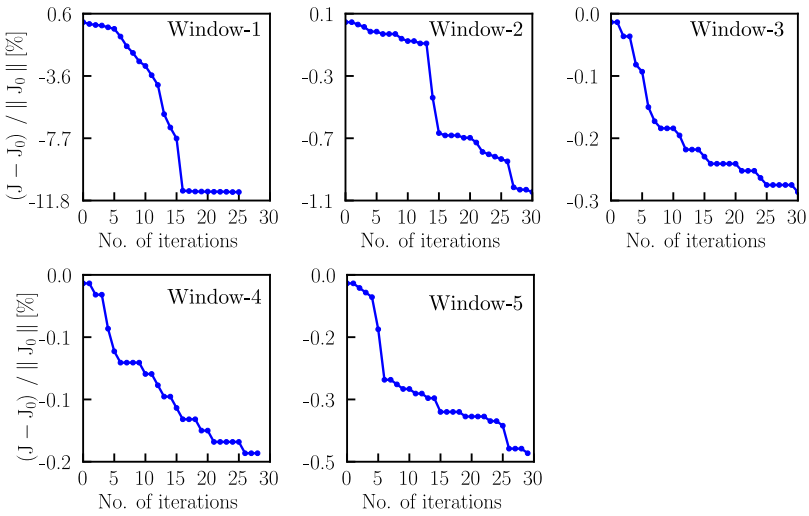

FIG. 4. Descent history of the cost function for sub-windows.

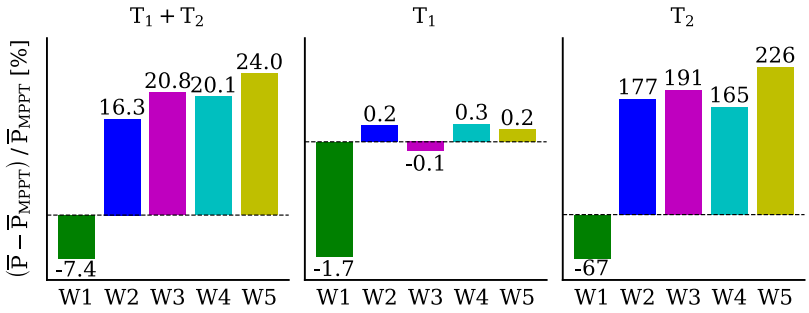

FIG. 5. Time averaged power gains for the optimization windows (W1-5). T1 and T2 are the upstream and the downstream wind turbines, respectively.

two different axial spacings between the rotors are considered, i.e., 5D (same as the above) and 3D. Finally, we also perform simulations on a grid that is twice refined in each direction, i.e., with $768 \times 384 \times 768$ grid points.

IV. RESULTS AND DISCUSSION

First, in Sec. IV A, the results from the optimal control case with uniform inflow are discussed, showing significant gains in energy extraction. Moreover, synthetic easy-to-use open-loop control signals are identified for further testing. Then, in Sec. IV B, we use the most performing signal to identify the flow physics that lead to increased energy extraction, in particular, focusing on the vortex dynamics in the wake. Subsequently, in Sec. IV C, we further apply the synthetic control signal to various cases with turbulent inflow to check its robustness and range of applicability. Finally, we conduct a grid refinement study in Sec. IV D. Note that in the rest of the text, T1 and T2 will be used for denoting the upstream and the downstream rotors, respectively.

A. Optimal control with uniform inflow

Here, we consider optimal control of two turbines using uniform inflow without any background perturbations. Several simulation studies thus far have already investigated turbine wake behavior for very low inflow turbulence intensities, focusing on near-wake behavior and tip-vortex dynamics[48–50] and showing that laminar-to-turbulence transition in the wake is significantly delayed when background turbulence is absent.[51,52] Thus, we can expect significant wake deficits at the second turbine, leading to low extraction efficiency and allowing for plenty of margin for control optimization. Moreover, as will be illustrated below, the clean undisturbed inflow leads to well-structured optimal control signals that can be easily reproduced. We should remark that the atmospheric boundary layer is usually turbulent, and we will test our control signals using turbulent inflow in Sec. IV C. Nevertheless, low turbulence conditions can also occur, e.g., in situations with shallow atmospheric boundary layers, or in the presence of stable stratification.

In Fig. 5, an overview is provided of the optimal control gains per window and per turbine, compared to the standard MPPT control. It is appreciated that the majority of the power gain comes from T2, while there is no significant change in generation of T1. We further see that in the first control window the gain is negative. This is related to the start-up of the optimal control and the transition from the MPPT to optimal control. When averaging the gains of windows 2–5, we find an overall gain of 20%. The overall gain in T2 is 190%.

In Fig. 6, we compare the control signals of the optimal control cases and the MPPT control, and further also compare power and rotational speed signals. First of all, looking at the MPPT signals, we observe that there are no variations in the controls of T1, as it experiences uniform inflow, while variations in T2 remain very moderate. Moreover, both for T1 and T2, $\beta = -1$, as this is the MPPT set point for the pitch angle.

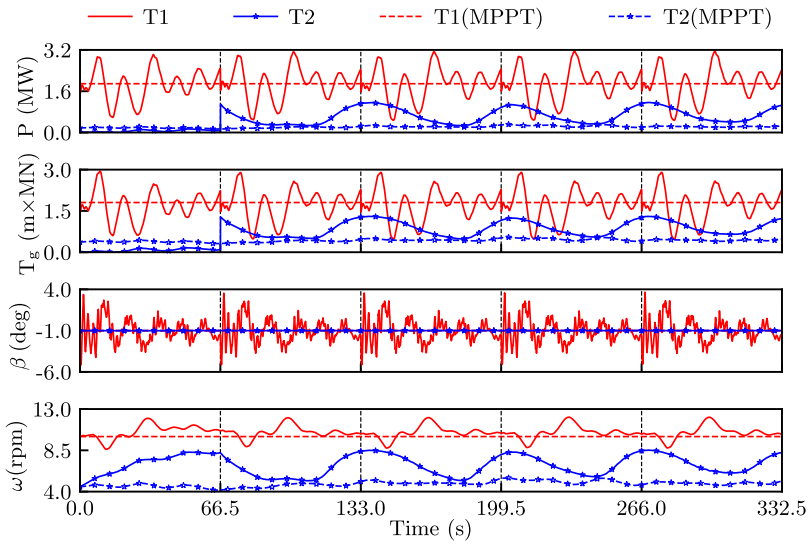

FIG. 6. Optimal control versus maximum power-point tracking (MPPT) control for uniform inflow conditions. Comparison of power (P), generator torque (T_g), blade pitch angle (β), and rotational speed (ω) trajectories of upstream (T1) and downstream (T2) wind turbines.

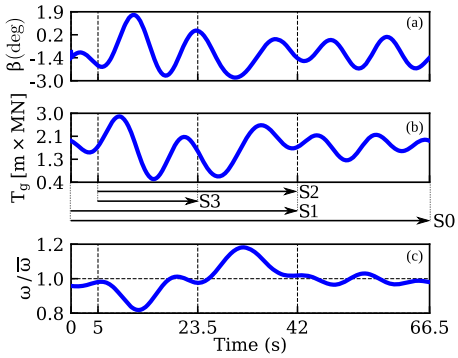

FIG. 7. The minimal optimal control signals (S0) for T1 and their derivatives (S1-S3) are shown in (a) and (b). The rotational speed trajectory in response to S0 is plotted in (c). Control signals longer than 66.5 s are obtained by periodic application of the above control signals.

When looking at the optimal control signals, we observe a lot of activity, in particular, in T1. As we will further illustrate below (see Sec. IV B), this leads to increased wake mixing and higher velocities at T2. Both generator torque and pitch are actuated in T1, and both signals repeat themselves per control window. This is logical, since inflow is uniform, so no adaptation to turbulent background fluctuations is necessary. We finally observe that the pitch-control signal of T1 has a very noisy high-frequency component. This is not a physically relevant result, and as further shown, these high frequencies can be filtered away without deteriorating the control effectiveness. This noisiness is introduced in the optimization by the relatively coarse LES mesh over which the blades rotate, leading to locally non-smooth interpolated inflow velocity at the blades. Possible solutions to this problem may include different smoothing and interpolation approaches in the ALM or the use of Sobolev smoothing of the gradient (see, e.g., Ref. 53). Both are topics of further research.

In Fig. 6, it is noticed that the power output of the optimally controlled upstream rotor regularly attains levels greater than that of the MPPT controlled counterpart. This is achieved by using the energy stored in the inertia. Looking at Fig. 6, it can be observed that the overshoots in the power production are accompanied by an increase in the generator torque and a decrease in the rotational speed. This is on average balanced at other time instances by the opposite action, that is, a decrease in generator torque and speedup of the rotor.

Looking at the optimal control of T2 in Fig. 6, we observe much smoother control signals than for T1. The power is periodically fluctuating, leading on average to a higher power output for T2. This is accompanied by a torque control signal that is in phase with the power fluctuations, while pitch is not actuated. Likewise, the rotational speed is periodically fluctuating, also in phase with the power signal. This behavior is the result of a periodically varying inflow velocity at T2 that is on average higher than for the uncoordinated case (see further discussion below). The T2 controls simply keep the turbine at its optimal tip-speed ratio given this velocity variation. In fact, replacing the T2 controls in the optimal-control problem with a MPPT strategy (for T2 only) leads to similar power gains.

We now further analyze the controls of T1 and derive four simpler control strategies for more practical use. Since the optimal controls of T1 are periodic and repetitive per window, we start by taking the controls of the fifth window. Subsequently, we remove the high-frequency components in the pitch control (cf. discussion above) by using a low-pass filter: to this end, the smoothed signal has been constructed by using the first seven harmonics of the original signal. For the sake of consistency, the same is also applied to the generator torque signal (although smoothing is not necessary). We denote these control signals as S0 (see Fig. 7).

Looking at S0 in Fig. 7, it is observed that the control amplitude gradually decreases toward the end of the time window. Moreover, in the last 25 s of the window, the impact on the rotational speed of the optimal control case (also shown in Fig. 7) is limited. We believe that this is related to finite horizon effects: the later a T1 control action occurs in the optimization time window, the less it can lead to power increases in T2, and thus, the optimal controller gradually returns to a greedy MPPT control strategy over the control time horizon. Therefore, we construct additional signals by shortening the S0 signal. To make the selection of these signals, we base ourselves on the rotational speed behavior.

Looking at the rotational speed in Fig. 7 in the first 42 s, a slowdown and speed-up is observed that is roughly antisymmetrical around 23.5 s and the average rotational speed. Therefore, a signal S1 is selected that corresponds to the first 42 s of S0, cutting away the last 24.5 s. A third signal S2 is constructed by further removing the first 5 s from S1, as control action and rotational speed fluctuations are very limited in this period. Finally, a last signal (S3) is constructed by taking the first half of S2. This last signal does only contain the first part of the antisymmetric rotational speed behavior mentioned above.

From a physical point of view, periodic optimal control signals can be expected as the flow is uniform and time invariant. Therefore, we periodically use these four control

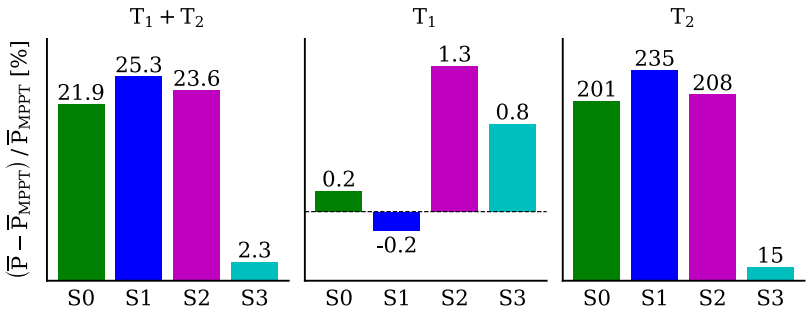

FIG. 8. Time averaged power gains associated with four different control signals (S0-S3) applied to the upstream wind turbine (T1). In all cases, the downstream with turbine (T2) is controlled with a maximum power point tracking algorithm.

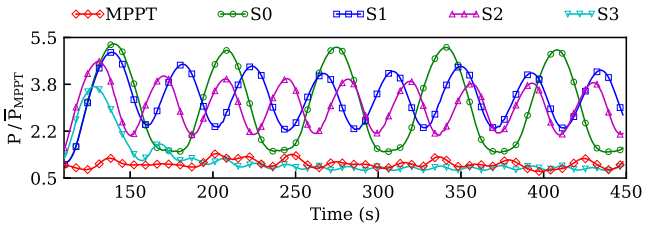

FIG. 9. Generation history of the downstream wind turbine (T2) in the wake of the upstream wind turbine (T1). T1 is controlled in five different ways: Either one of the S0-S3 is applied, or the maximum power point tracking (MPPT) algorithm is employed. In all cases, T2 is MPPT controlled.

signals in a set of simulations over a longer time horizon of 450 s so that we obtain accurate statistical averages on power gains. For the second turbine, we simply use a MPPT controller, as suggested by the optimal control behavior of T2. Moreover, as a reference, we use the MPPT controller for both turbines also simulated over the longer time horizon of 450 s.

Results on power gains relative to the standard MPPT control are shown in Fig. 8. It is found that the signals S0, S1, and S2 achieve significant total power gains over the MPPT controller, reaching similar levels as previously observed for the optimal controller. Overall, S1 performs best with a power extraction that is even slightly higher than observed for the optimal controller in Fig. 5. Remark that this difference is statistically not significant in view of the relatively short time horizons available for averaging in the optimal control case. It is further observed in Fig. 8 that the signal S3 is not successful at all, showing that the antisymmetric behavior in rotational speed observed above is an essential feature of the control mechanism.

The gains in T2 (which is controlled using a MPPT controller) are further investigated by looking at the power history of T2 for the different control signals S0–S3 in Fig. 9. Again it is appreciated that S3 is not effective, while the other signals lead to a strongly increased power extraction that periodically oscillates. Since the signals S0–S2 are all constructed by periodic repetition of basis signals with different length, the excitation frequency of these cases is different and corresponds to a Strouhal number of $St = 0.237$, $St = 0.375$, and $St = 0.426$, respectively [with $St = D/(\tau U_\infty)$ and τ being the period of the control signals]. This is also clearly visible in Fig. 9 when looking at the period of the power extraction of T2.

Overall, the signal S1 performs best in terms of power gains, as well as in terms of simplicity of the signal. In Subsection IV B, we investigate in more detail the wake field of T1 associated with the periodic application of the control signal S1. Three periods of the S1 signal as well as its frequency domain representation are given in Fig. 10. Remember that the S1 signal is cut out from the S0 signal (see Fig. 7); hence, notice that the overall signal is mildly discontinuous at the connection points. Next, in Sec. IV C, we investigate the robustness of the results for different turbulent inflow conditions.

B. Visualization of control physics for signal S1

We now further investigate the simulation results for the signal S1. To this end, we look at snapshots of the axial velocity in the wake of T1 in Fig. 11(a). Moreover, in Fig. 11(b), the kinetic energy E_k in the wake of T1 is shown as a function of time, where

$$E_k(t) = \int_0^{5D}\int_0^{2\pi}\int_0^{R} \frac{1}{2}\left(\tilde{u}_1^2 + \tilde{u}_2^2 + \tilde{u}_3^2\right) dx_1 d\theta dr. \qquad (21)$$

In Fig. 11, we start applying the signal S1 at $t = 0$. Before this, the standard MPPT controller was used for T1, leading to a strong wake behind T1 that impinges on T2. Note that the flow remains largely laminar in the wake of T1 at $t = 0$. Transition only starts around $x = 3.5D$, and the flow is fully turbulent only in the wake of T2. This is clearly related to the uniform unperturbed inflow conditions that are used in these simulations. We remark that predicting the exact location of the transition using LES is nontrivial and depends strongly on the grid resolution (see below for a further grid sensitivity study), as the initial transition happens at small scales in the thin shear layer between the wake and free stream. In Sec. IV C, we investigate turbulent inflows, for which wake transition is not an issue.

Looking at the velocity field in subsequent snapshots in Fig. 11, we observe that high speed flow is entrained into the wake (cf. $t = 50$–112 s). The process starts with a perturbation of the shear layer and continues with penetration of high-speed flow into the inner core of the wake. Eventually, the high-speed flow reaches the center of the wake, breaking up the wake.

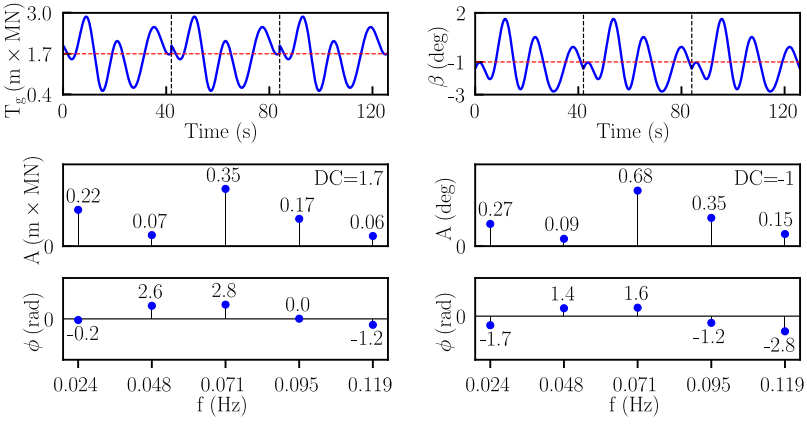

FIG. 10. Time and frequency domain representations of the S1 signal (left column: generator torque, right column: blade pitch). On the top row, three periods of the S1 signal is shown (horizontal dashed line: mean). On the second and the third rows, the amplitudes and the phases of the first five harmonics of the S1 signal are shown, respectively.

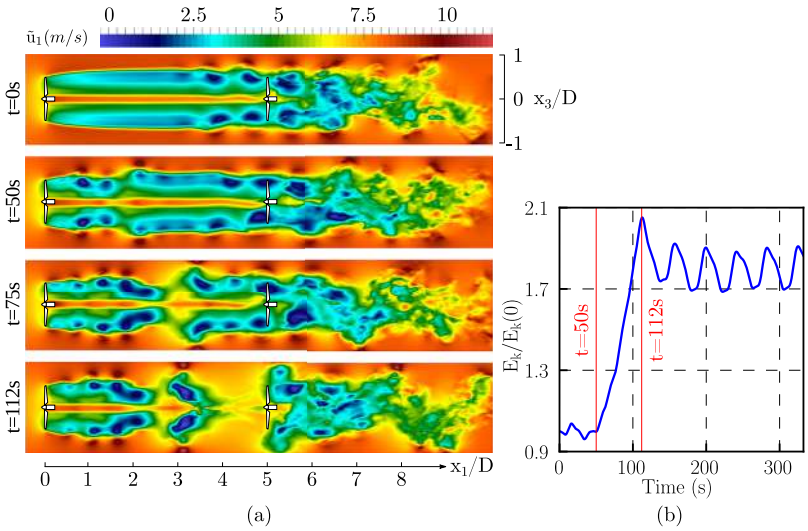

FIG. 11. (a) Axial velocity contours at four different time instants of the wake evolution in response to the control signal S1. (b) Spatially integrated kinetic energy $E_k(t)$ in the wake of T1 as a function of time (normalized by the kinetic energy at $t = 0$ s).

As a result, three zones emerge: a low-speed zone attached to T1, which can be considered as T1's new shorter wake, a detached low-speed zone farther downstream, and a high speed zone in between. After the breakup of the wake, the penetration of high-speed flow into the wake core continues. This causes the detached zone to be pushed further downstream and slightly radially outward, while the advection of the attached zone is retarded. As a result, the axial extent of the high speed zone enlarges. Eventually, the high-speed zone leads to increased energy extraction when it arrives at T2. The periodic application of signal S1 leads to a periodic repetition of this process, explaining the power signal observed for T2 in Fig. 9. This is further quantified in Fig. 11(b), showing the spatially integrated kinetic energy in the wake of T1 as a function of time. It is observed that the energy in the wake starts to increase drastically at $t = 50$ s, which corresponds to the onset of high-speed flow penetration in Fig. 11(a). The energy in the wake increases until $t = 112$ s, after which it starts oscillating around a level which is approximately 1.8 times higher than the initial state.

In Fig. 12 (Multimedia view), the vortex structures in the wake of T1 controlled using signal S1 are visualized using the Q criterion[54] showing snapshots from $t = 116$ s to $t = 224$ s, corresponding approximately to 2.5 periods of actuation with signal S1. The axial velocity field is also shown in color in the figure. We observe that T1's wake is strongly dominated by coherent vortex rings. This is different from the classical helical tip vortex system that is observed in the conventional operation of wind turbines,[55] although a helical tip-vortex system can still be observed close to the turbines in some snapshots (see, e.g., at $t = 224$ s for T2).

We find that the successive application of signal S1 leads to the emergence of three consecutive vortex rings over one period, which we label with letters A, B, and C in Fig. 12 (Multimedia view). The wake energizing process is driven by the strong mutual interaction between those three vortex rings. The interaction resembles a typical leap-frogging phenomenon, which is commonly observed between two coaxial vortex rings, traveling in the same direction.[56–58] Here, the interaction occurs between three vortex rings. This can be

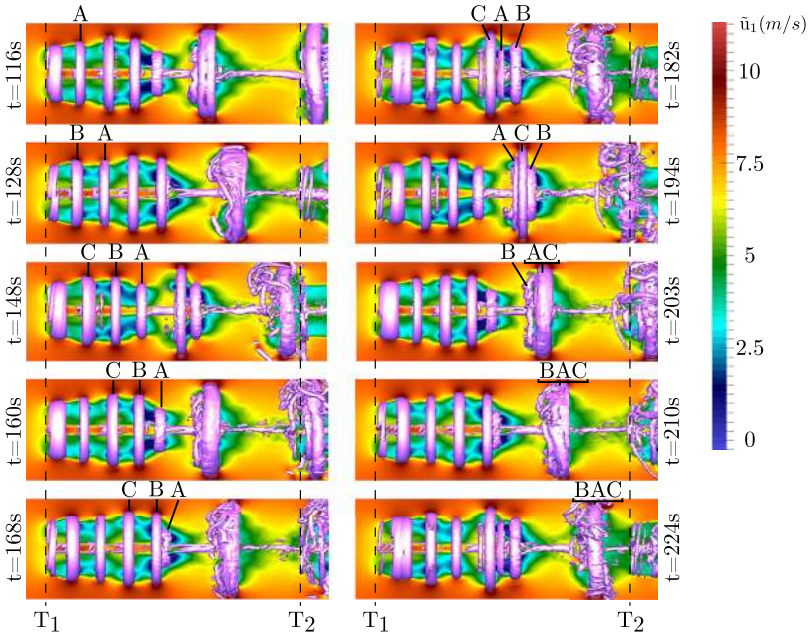

FIG. 12. Visualization of the coherent structures when the upstream rotor is controlled using signal S1. In color: axial velocity field. Vortex structures are visualized using the Q-criterion, showing isosurfaces of $Q = 0.01$ s^{-2}. T1 and T2 mark the axial locations of the upstream and the downstream wind turbines, respectively. Multimedia view: https://doi.org/10.1063/1.5038600.1

observed from 160 to 224 s: the leading vortex ring A shrinks under the effect of the induced velocity field of ring B. Moreover, ring A decelerates because of the induced velocity field by ring B, as well as its own self-induced velocity which is increased due to shrinking. Meanwhile, ring B expands and accelerates. Eventually, ring B overtakes ring A as seen at t = 182 s. Subsequently, ring A is also overtaken by ring C (t = 194 s), after which it merges with ring C into a larger ring AC (t = 203 s). Finally, ring B now also shrinks under the effect of the induced velocity field of ring AC, is subsequently overtaken by ring AC (t = 203 s), and finally merges with AC to form ring BAC (t = 210 s).

As observed in Fig. 12 (Multimedia view), the induced velocity fields from rings A, B, and C and their merging lead to strong entrainment of high-speed velocity in front of the merged rings, explaining the observations in Fig. 11. The periodic application of signal S1 leads to the periodic excitation of such a three-vortex system, and this is also visible in Fig. 12 (Multimedia view) (t = 116 s), where three prior triples to the BAC system are visible, with the two most downstream of them already merged into single large vortices.

In Fig. 13, the blade pitch angle, the rotational speed, and the disk-based thrust coefficient along with the vortex shedding [cf. Fig. 12 (Multimedia view)] intervals are shown for a period of the control signal. The thrust coefficient in the figure is based on the rotor-averaged axial velocity ($\widetilde{u}_d$) and reads

$$C_T' = \frac{F_1}{1/2\rho\widetilde{u}_d^2 A}, \tag{22}$$

with $A = \pi R^2$ being the rotor swept area. Notice that the generator torque signal is not plotted in Fig. 13 as it does not affect the flow directly, but only through the rotational speed. It is evident that the triple vortex system emerges as a result of the alternating control pattern. That is, each vortex ring is created during the course of an increase in the thrust coefficient, preceded by a relaxation. Looking into more details at our results, we found that the increase of the thrust coefficient was mainly located near the outer part of the blade, also increasing the tip vortex strength. These tip vortices then merge together into one single vortex ring.

A recent optimal wind farm control study by Munters and Meyers[19] used actuator disk models, using C_T', which directly appears in the ADM as a control parameter. When focusing on the first row in the farm, similar alternating control patterns were observed, including the formation of vortex rings. However, during one period of excitation, only one vortex ring was formed at a Strouhal number of 0.25, compared to 0.375 used here. We attribute these differences to (1) the turbine models (e.g., a different radial force distribution), (2) the finer resolution, as well as (3) more realistic control parameters, and the inclusion of turbine inertia in the current study.

Regarding the other control signals, the application of S0 and S2 to T1 also leads to vortex dynamics and wake energizing processes that are similar to the ones described earlier for S1 (not shown). The S3 signal excites only two vortex rings, which also mutually interact and eventually merge as shown in Fig. 14. However, in this case, the interaction is not strong enough to entrain sufficient free-stream energy into the wake, and the S3 control signal does not perform any better than the MPPT control (cf. Fig. 9).

C. Turbulent inflow

In this section, signal S1 is further tested for different turbulent inflow conditions and for a turbine spacing of 5D (same as before), as well as a spacing of 3D. Again, we have a reference case where both turbines are controlled with the MPPT algorithm, and next to that a case with T1 periodically using signal S1, and T2 using MPPT. Turbulent inflow conditions with various turbulence intensities (TI = 1%, 5%, and 10%) and length scales (L = 8 m, 15 m, 30 m, and 63 m) are considered. To this end, turbulent fluctuations are generated in Tugen and then superimposed on a uniform inflow with a velocity of 8 m/s.

An overview of the different cases and the respective gains is provided in Table I. Next to the turbulence intensity and length scale at the inlet, the table also lists the turbulence intensity on the plane of the upstream rotor, significantly outside the rotor swept area (y/D = 5.5). Since turbulence at the inlet is imposed on a uniform background flow, there is no production outside the rotor affected region, so that turbulence slowly decays, with larger decay rates for smaller length

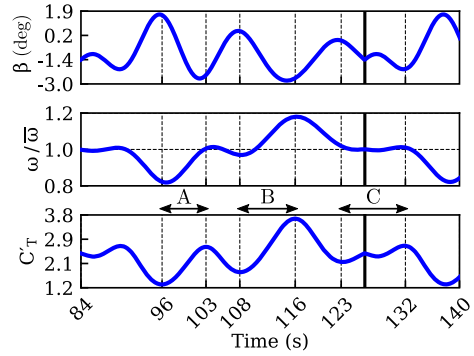

FIG. 13. The connection of vortex-shedding of T1 with signal S1. Top to bottom: blade pitch angle, rotor speed, and thrust coefficient. A, B, and C denote the intervals during which the respective vortex rings in Fig. 12 (Multimedia view) are formed. The interval between t = 84 s and the vertical solid line corresponds to one period of the control signal.

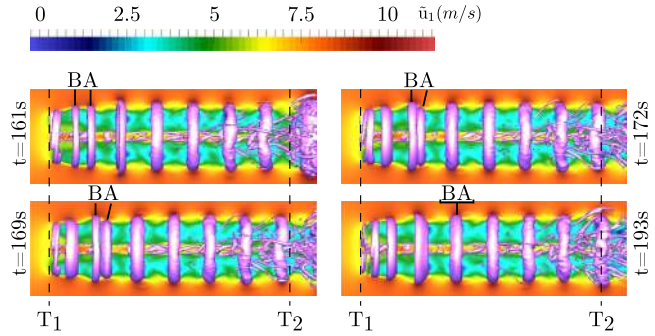

FIG. 14. Visualization of the coherent structures when the upstream rotor is controlled using signal S3. In color: axial velocity field. Vortex structures are visualized using the Q-criterion, showing isosurfaces of Q = 0.01 s^{-2}. T1 and T2 mark the axial locations of the upstream and the downstream wind turbines, respectively.

TABLE I. Time averaged power gains (%) associated with the employment of the optimal controls for the upstream wind turbine, while the downstream wind turbine employs the maximum power point tracking (MPPT) algorithm. Gains are computed with respect to a reference case, in which both wind turbines are MPPT controlled. Results are presented for two different axial spacings between the rotors (i.e., 3D and 5D) and for various turbulent inflow conditions. TI and L are the turbulence intensity and the integral length scale at the domain inlet, respectively, and TI^* is the turbulence intensity at the rotor plane, well out of the rotor swept area (y/D = 5.5).

			3D			5D		
TI (%)	TI^* (%)	L (m)	T1	T2	T1 + T2	T1	T2	T1 + T2
1	0.90	8	0.0	137.8	12.6	0.0	77.0	15.6
1	0.95	15	−0.2	110.1	11.4	−0.2	56.8	12.2
1	0.98	30	−0.4	88.0	9.9	−0.4	46.1	10.1
1	1	63	−0.4	83.2	9.3	−0.4	46.1	10.2
5	3.3	8	−0.5	70.7	7.9	−0.5	49.2	9.7
5	3.8	15	−0.7	31.9	3.9	−0.7	30.6	6.3
5	4.3	30	−0.8	12.8	1.4	−0.8	7.8	1.4
5	4.8	63	−1.4	7.7	0.2	−1.4	3.2	−0.2
10	5.2	8	−0.7	45.4	5.2	−0.7	35.0	6.9
10	6.6	15	−0.7	9.2	0.9	−0.7	9.5	1.8
10	7.9	30	−0.9	−4.9	−1.6	−0.9	−0.8	−0.9
10	9.2	63	−2.4	−4.6	−2.9	−2.4	−0.6	−1.8

scales. Also, the decay rate of turbulence gets larger as the inflow turbulence intensity increases.

When looking at the gains in Table I for the same turbulence length scales, it is seen that the effectiveness of the control disappears for higher turbulence intensities. Comparing 3D and 5D spacings, we observe that gains are slightly larger for the higher spacing (for which the signal S1 was optimized earlier), but differences are not very big. Finally, in cases where power gains are significant, it is seen that the application of signal S1 to T1 leads to a substantial increase in T2's generation, while its effect on T1's output is rather smaller. This is in line with the earlier results for the non-turbulent inflow case.

The decrease of control efficiency with turbulence intensity can be attributed to two effects. First of all, higher turbulence levels lead to improved wake mixing, decreasing the margins for improvement of control strategies. Second, the signal S1 is designed for a non-turbulent background flow. The latter is appreciated when looking at the vorticity dynamics of the S1 controlled case in Fig. 15 for TI_{in} = 5% and L_{in} = 15 m. For this case, gains are still around 6% compared to MPPT. It is seen that the coherent vortex rings are still recognizable in the near wake, but significantly distorted. Further downstream, the vortex rings break up and evolve toward quasi-streamwise vortex tubes, and coherence is gradually lost. This reduces the effectiveness of the control. It is evident that the presence of background turbulence accelerates the disintegration of coherent vortex rings, and this is even more the case for higher turbulence levels.

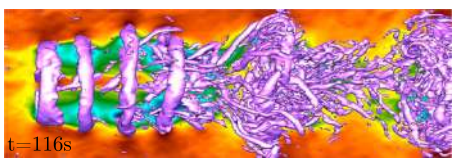

FIG. 15. A snapshot of the vortical flow field emerging for the control signal S1 applied to the upstream wind turbine and turbulent inflow conditions TI_{in} = 5% and L_{in} = 15 m.

In the study by Munters and Meyers,[19] the optimal control signals are found to be effective at higher turbulence intensities (i.e., they obtained a 2% power gain with an inflow turbulence intensity of 16%). However, this was achieved with a larger control amplitude for C'_T ($0.5 < C'_T < 3.5$ in the work of Munters and Meyers[19] versus $1.2 < C'_T < 3.8$) here. Next to that, model detail and grid resolution can also play an important role. Therefore, the comparison of the two wind turbine models in the context of dynamic wind-farm control remains an important topic for future research.

D. Grid refinement study

Up until now, all simulations were performed on a grid of approximately 28×10^6 cells, a size that was mainly dictated by the computational resources available for the optimal control case in Sec. IV A. Here, we refine the mesh with a factor two in each direction for a selection of four cases, i.e., one with uniform inflow and one with turbulent inflow (TI_{in} = 5% and L_{in} = 15 m), each time for the MPPT case and for T1 controlled using signal S1. This yields a grid resolution of 2.3 m × 2 m × 1 m for a total of approximately 225×10^6 cells and ($R/\Delta \approx$) 37 LES grid points per actuator line, which complies with typical resolution requirements for ALM in LES.[44]

The results are shown in Figs. 16 and 17. First of all, in Fig. 16, the axial velocity is shown at different downstream distances from the first turbine for the two grids and the reference case. It is observed that velocity profiles collapse very well for both grids. The largest discrepancy can be found for the non-turbulent inflow case, for which some differences

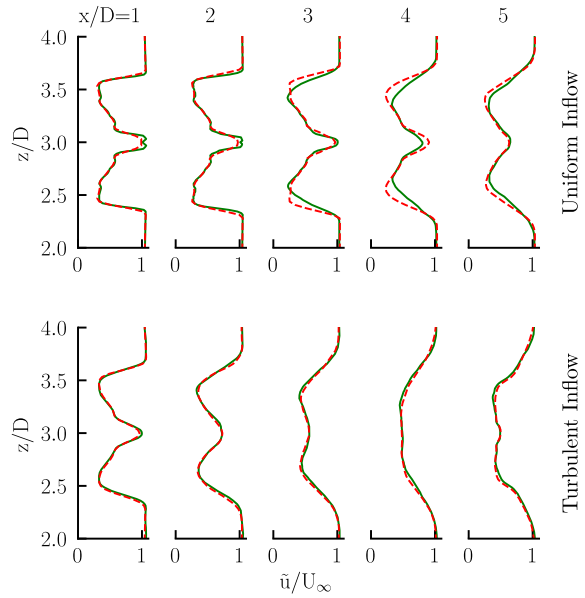

FIG. 16. Comparison of the axial velocity profiles under two different inflow conditions and on two different grid resolutions (dashed line: coarse grid; solid line: fine grid). Both rotors are controlled with the MPPT algorithm.

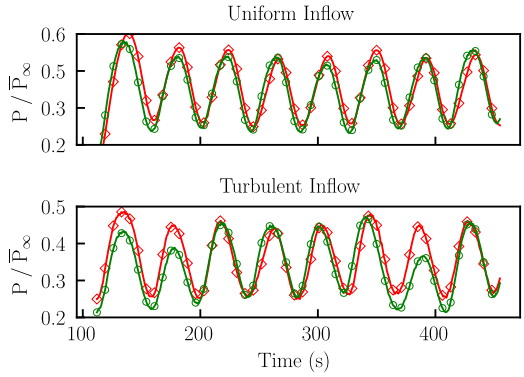

FIG. 17. Grid refinement study. Comparisons of the downstream rotor's power output under two different inflow conditions and on two different grid resolutions (lines with diamonds: coarse grid; lines with circles: fine grid). The upstream rotor employs S1 control signal, while the downstream rotor is controlled with the MPPT algorithm.

are visible at the wake edge 3D and 4D downstream of T1. This is related to the fact that the laminar-to-turbulent transition in the thin shear-layer at the edge of the turbine wake starts at very small scales, and the grid is not yet sufficiently refined to capture these details. However, at all other locations, as well as for the turbulent inflow case, this is no issue.

In Fig. 17, the power output of the downstream wind turbine (as a function of time) is compared for the two grids, the laminar and turbulent inflow case. In both cases, the upstream rotor employs signal S1, while the downstream rotor is controlled with the MPPT algorithm. First of all, we observe that the power output for the laminar inflow case is very similar for both grids in spite of the grid dependency of the transition location. For the turbulent inflow case, differences are sometimes larger (e.g., between 100 and 200 s or around 400 s), but overall results collapse relatively well. Moreover, differences can be explained by instantaneous difference in turbulent realizations. Although the turbulent inflow fields for both grids are characterized by the same average turbulence intensity and the integral length scale at the inlet, the two turbulent fields are not exactly the same.

Overall, we conclude that the control signals and mechanisms identified above are independent of the grid resolution. This makes also sense from a numerical point of view, since the wake energizing process described in Secs. IV A–IV C develops on a length scale comparable to the rotor diameter, which is considerably larger than the grid resolutions we used in our simulations.

V. CONCLUSIONS

We investigated dynamic induction control for mitigating the wake losses of a pair of inline NREL 5 MW turbines. To this end, we combined optimal control with large-eddy simulations. Using adjoint-based optimization in a receding horizon setting, the turbine controls were optimized for maximum power production.

The optimal control setup consists of two inline NREL-5 MW rotors, which are separated by five rotor diameters in the streamwise direction and represented with an actuator line model. The turbine controls were optimized under uniform non-turbulent inflow conditions so as to investigate the turbine induced wake energizing process in the absence of background turbulence. Subsequently, the optimal control results were compared to a standard MPPT control in a similar setup, and power gains of about 25% were found for the optimal control scenario in this particular case. We further found that the optimal control mainly changes the control dynamics of the first turbine, improving wake mixing, while the control of the second turbine remains close to a simple MPPT controller.

Based on the generator torque and pitch signals of the optimal control case, we derived a simplified control signal for the first turbine, which can be periodically used as an open-loop controller with a Strouhal number of 0.38. Using a MPPT controller for the second turbine, we find that gains remain in the order of 25% for the uniform inflow case. The wake mixing mechanisms were further investigated, and it was found that the T1 controller periodically sheds three vortex rings, which interact downstream and eventually merge into one big vortex ring, enhancing entrainment of free-stream momentum in front of the ring.

The vortex rings emerge in phase with an increase in the rotational speed and a decrease in the blade pitch angle, which leads to a combined effect of increased disk-based thrust coefficient. The resulting vortex dynamics is different than the one observed earlier by Munters and Meyers[19] using an ADM model and direct control of the disk-based thrust-coefficient. Possible causes are attributed to the finer resolution in the current ALM simulations, the different turbine representation, including the effect of rotor inertia, and the radial distribution of forces in the ALM.

The control signals developed for uniform non-turbulent inflow were further tested for turbulent inflow conditions and two different turbine spacings, namely, 3D and 5D. We observed that the power gains are slightly higher for larger spacing. On the other hand, turbulent inflow conditions have a remarkable impact on the obtained power gains. In general, the power gains were observed to decrease with increasing turbulence intensity and integral length scale. For approximately 1% of inflow turbulence intensity with an integral length scale of 8 m and 63 m, the power gains were found to be 15.6% and 10.2%, respectively. In the case of 3%–4% of inflow turbulence intensity with an integral length scale of 8 m and 30 m, power gains were found to be 9.7% and 1.4%, respectively. Finally, for 5%–6.5% of inflow turbulence intensity with an integral length scale of 8 m and 15 m, power gains were observed to be around 7% and 2%, respectively. For higher turbulence levels, the control signal loses its effectiveness, as now the vortex rings break up and lose their coherence very fast. Moreover, higher turbulence levels naturally lead to improved wake mixing also in the MPPT case so that there is less room for improvement.

Compared to earlier optimal control studies using an ADM approach, we observed that ALM increases the numerical complexity of the adjoint-based receding-horizon optimization. We found this to be related to the rotational position equation and the numerical noise that is generated by actuator forces that rotate over the LES grid. To improve convergence, we formulated a discrete adjoint Runge–Kutta method.

Unfortunately, this does not remove all numerical noise and restricted the use of our optimal control simulations to non-turbulent inflow cases. Future work will need to look into improving our algorithms by, e.g., adapting ALM interpolation[60–62] and filtering, introducing Sobolev smoothing of the gradients or considering different optimization methods such as thrust region methods, among others.

Finally, while we identified a new physical control mechanism that can be used to improve wake mixing of wind-turbine wakes, the robustness of the S1 signal is still to be checked with more than two rows of turbines. Moreover, practical feasibility also depends on the additional aspects related to structural loads and lifetime of different components of the turbine. These require further research.

ACKNOWLEDGMENTS

The authors acknowledge financial support from the European Research Council (ERC Grant No. 306471) and the Flemish Science Foundation (FWO, Grant No. G.0376.12). The computational resources and services used in this work were provided by the VSC (Flemish Supercomputer Center), funded by the Research Foundation Flanders (FWO) and the Flemish Government—Department EWI.

APPENDIX A: DERIVATION OF THE ADJOINT EQUATIONS

In the current appendix, the derivation of the adjoint equations is presented. To this end, first proper inner products are defined for control and state variables, i.e.,

$$(\boldsymbol{\varphi}_1, \boldsymbol{\varphi}_1) = \int_0^T (\boldsymbol{T}_{g1} \cdot \boldsymbol{T}_{g2} + \boldsymbol{\beta}_1 \cdot \boldsymbol{\beta}_2)\, \mathrm{d}t, \tag{A1}$$

$$(\boldsymbol{q}_1, \boldsymbol{q}_1) = \int_0^T \int_\Omega \boldsymbol{u}_1 \cdot \boldsymbol{u}_2 \, \mathrm{d}\boldsymbol{x}\mathrm{d}t + \int_0^T \int_\Omega p_1 p_2 \, \mathrm{d}\boldsymbol{x}\mathrm{d}t + \int_0^T (\boldsymbol{\theta}_1 \cdot \boldsymbol{\theta}_2 + \boldsymbol{\omega}_1 \cdot \boldsymbol{\omega}_2)\, \mathrm{d}t. \tag{A2}$$

Similar inner products follow for elements of $\boldsymbol{\varphi}$ and $\boldsymbol{q}$. For instance, the inner product for the velocity field corresponds to the first term on the right-hand side of Eq. (A2).

In order to derive the adjoint equations, we follow the classical Lagrangian approach. Using the Lagrange multipliers $\boldsymbol{q}^* = [\boldsymbol{\xi}(\boldsymbol{x}, t), \pi(\boldsymbol{x}, t), \boldsymbol{\chi}(t), \boldsymbol{\Upsilon}(t)]$, we formulate the Lagrangian as

$$\begin{aligned}\mathscr{L}(\boldsymbol{\varphi}, \boldsymbol{q}, \boldsymbol{q}^*) = \mathscr{J}(\boldsymbol{\varphi}, \boldsymbol{q}) &+ \int_0^T \int_\Omega \pi \nabla \cdot \widetilde{\boldsymbol{u}} \, \mathrm{d}\boldsymbol{x}\mathrm{d}t \\ &+ \int_0^T \int_\Omega \left(\frac{\partial \widetilde{\boldsymbol{u}}}{\partial t} + \widetilde{\boldsymbol{u}} \cdot \nabla \widetilde{\boldsymbol{u}} + \frac{1}{\rho} \nabla \widetilde{p} + \nabla \cdot \boldsymbol{\tau} - \boldsymbol{f} \right) \cdot \boldsymbol{\xi} \, \mathrm{d}\boldsymbol{x}\mathrm{d}t \\ &+ \int_0^T \left(\frac{\mathrm{d}\boldsymbol{\omega}}{\mathrm{d}t} - \frac{\boldsymbol{T}_a - \boldsymbol{T}_g}{J} \right) \cdot \boldsymbol{\chi} \, \mathrm{d}t, \\ &+ \int_0^T \left(\frac{\mathrm{d}\boldsymbol{\theta}}{\mathrm{d}t} - \boldsymbol{\omega} \right) \cdot \boldsymbol{\Upsilon} \, \mathrm{d}t, \end{aligned} \tag{A3}$$

where $\boldsymbol{\xi}$, $\boldsymbol{\chi}$, and $\boldsymbol{\Upsilon}$ are tensors with the same dimensions as $\widetilde{\boldsymbol{u}}$, $\boldsymbol{\omega}$, and $\boldsymbol{\theta}$, respectively.

If the proper adjoint equations are satisfied, the gradient of the reduced cost functional can now be identified as the Riesz representation of the Gateau differential of the Lagrangian to the control variables, i.e., $(\nabla \tilde{\mathscr{J}}, \delta\boldsymbol{\phi}) = \mathscr{L}_{\boldsymbol{\phi}}(\delta\boldsymbol{\phi})$. The adjoint equations are obtained by expressing the Riesz representation of $\mathscr{L}_{\boldsymbol{q}}(\delta\boldsymbol{q}) = 0$. Details of the underlying theory can be, e.g., found in Ref. 33, and, applied to optimal control in LES, in Ref. 15 (see Appendix C).

The derivation of the adjoint equations for the standard Navier–Stokes equations following the above procedure is well known and can be found in Refs. 23, 59, and 36 among others. Moreover, the derivation of the LES equations in a boundary-layer setting including the adjoint subgrid-scale model is documented in Ref. 15. Therefore, in the current appendix, we restrict ourselves to the derivation of the gradient of the reduced cost functional, and the adjoint ALM equations, which include adjoint equations for the turbine dynamics, as well as an adjoint forcing term in the adjoint momentum equation. These derivations are given in Appendixes A 1–A 5.

1. Gradient of the cost functional

First of all, using (A3), the derivation of the second part of the gradient $\nabla \tilde{\mathscr{J}}_T$ is straightforward. We obtain

$$\mathscr{L}_{\boldsymbol{T}_g}(\delta\boldsymbol{T}_g) = \int_0^T -\boldsymbol{\omega} \cdot \delta\boldsymbol{T}_g + \frac{\boldsymbol{\chi}}{J} \cdot \delta\boldsymbol{T}_g \, \mathrm{d}t \tag{A4}$$

so that $\nabla \tilde{\mathscr{J}}_T = -\boldsymbol{\omega} + \boldsymbol{\chi}/J$.

The derivation of $\nabla \tilde{\mathscr{J}}_\beta$ is more elaborate. We obtain

$$\begin{aligned}\mathscr{L}_{\boldsymbol{\beta}}(\delta\beta) &= \int_0^T \int_\Omega \left(-\frac{\mathrm{d}\boldsymbol{f}}{\mathrm{d}\boldsymbol{\beta}} \delta\boldsymbol{\beta} \right) \cdot \boldsymbol{\xi} \, \mathrm{d}\boldsymbol{x}\mathrm{d}t + \int_0^T \frac{1}{J} \left(-\frac{\mathrm{d}\boldsymbol{T}_a}{\mathrm{d}\boldsymbol{\beta}} \delta\boldsymbol{\beta} \right) \cdot \boldsymbol{\chi} \, \mathrm{d}t \\ &= \int_0^T \int_\Omega \left(\sum_{i,j} \int_0^1 G(\boldsymbol{x} - \boldsymbol{x}^{ij}(\mu)) \left(\frac{\mathrm{d}\boldsymbol{F}^{ij}}{\mathrm{d}\beta^i} \delta\beta^i \right) \mathrm{d}\mu \right) \cdot \boldsymbol{\xi} \, \mathrm{d}\boldsymbol{x}\mathrm{d}t + \int_0^T \frac{1}{J} \left(-\left[\frac{\mathrm{d}\boldsymbol{T}_a}{\mathrm{d}\boldsymbol{\beta}} \right]^* \boldsymbol{\chi} \right) \cdot \delta\boldsymbol{\beta} \, \mathrm{d}t \\ &= \int_0^T \left(\sum_{i,j} \int_0^1 \left(\frac{\mathrm{d}\boldsymbol{F}^{ij}}{\mathrm{d}\beta^i} \delta\beta^i \right) \cdot \left[\int_\Omega G(\boldsymbol{x} - \boldsymbol{x}^{ij}(\mu)) \boldsymbol{\xi} \, \mathrm{d}\boldsymbol{x} \right] \mathrm{d}\mu \right) \mathrm{d}t + \int_0^T \frac{1}{J} \left(-\left[\frac{\mathrm{d}\boldsymbol{T}_a}{\mathrm{d}\boldsymbol{\beta}} \right]^* \boldsymbol{\chi} \right) \cdot \delta\boldsymbol{\beta} \, \mathrm{d}t \\ &= \int_0^T \left(\sum_{i,j} \int_0^1 \frac{\mathrm{d}\boldsymbol{F}^{ij}}{\mathrm{d}\beta^i} \cdot \left(\int_\Omega G(\boldsymbol{x} - \boldsymbol{x}^{ij}(\mu)) \boldsymbol{\xi} \, \mathrm{d}\boldsymbol{x} \right) \mathrm{d}\mu \right) \delta\beta^i \, \mathrm{d}t + \int_0^T \frac{1}{J} \left(-\left[\frac{\mathrm{d}\boldsymbol{T}_a}{\mathrm{d}\boldsymbol{\beta}} \right]^* \boldsymbol{\chi} \right) \cdot \delta\boldsymbol{\beta} \, \mathrm{d}t \end{aligned} \tag{A5}$$

so that

$$\nabla\tilde{\mathscr{J}}_\beta = \sum_j \mathbf{1}_i \int_0^1 \frac{\mathrm{d}\boldsymbol{F}^{ij}}{\mathrm{d}\beta^i} \cdot \left(\int_\Omega G(\boldsymbol{x}-\boldsymbol{x}^{ij}(\mu))\boldsymbol{\xi}\,\mathrm{d}\boldsymbol{x}\right)\mathrm{d}\mu - \frac{1}{J}\left[\frac{\mathrm{d}\boldsymbol{T}_a}{\mathrm{d}\boldsymbol{\beta}}\right]^* \boldsymbol{\chi}, \tag{A6}$$

with $\mathbf{1}_i$ being the N_t-dimensional unit tensor in direction i.

Furthermore, the Jacobian $\mathrm{d}\boldsymbol{T}_a/\mathrm{d}\boldsymbol{\beta}$ is diagonal so that $[\mathrm{d}\boldsymbol{T}_a/\mathrm{d}\boldsymbol{\beta}]^* = \mathrm{d}\boldsymbol{T}_a/\mathrm{d}\boldsymbol{\beta}$. Further expressions for the Jacobians $\mathrm{d}\boldsymbol{T}_a/\mathrm{d}\boldsymbol{\beta}$ and $\mathrm{d}\boldsymbol{F}^{ij}/\mathrm{d}\beta^i$ are provided in Appendix A 5.

2. Adjoint equation of rotation

The adjoint rotation equation is obtained by casting $\mathscr{L}_{\boldsymbol{\omega}}(\delta\boldsymbol{\omega}) = 0$ in its Riesz representation form. We find

$$\begin{aligned}
\mathscr{L}_{\boldsymbol{\omega}}(\delta\boldsymbol{\omega}) &= \int_0^T -(\mathbb{T}+\boldsymbol{\Upsilon})\cdot\delta\boldsymbol{\omega} + \frac{\mathrm{d}\delta\boldsymbol{\omega}}{\mathrm{d}t}\cdot\boldsymbol{\chi} - \frac{1}{J}\left(\frac{\mathrm{d}\boldsymbol{T}_a}{\mathrm{d}\boldsymbol{\omega}}\delta\boldsymbol{\omega}\right)\cdot\boldsymbol{\chi}\,\mathrm{d}t - \int_0^T\int_\Omega \frac{\mathrm{d}\boldsymbol{f}}{\mathrm{d}\boldsymbol{\omega}}\delta\boldsymbol{\omega}\cdot\boldsymbol{\xi}\,\mathrm{d}\boldsymbol{x}\mathrm{d}t \\
&= \int_0^T -(\mathbb{T}+\boldsymbol{\Upsilon})\cdot\delta\boldsymbol{\omega} - \frac{\mathrm{d}\boldsymbol{\chi}}{\mathrm{d}t}\cdot\delta\boldsymbol{\omega}\,\mathrm{d}t + \boldsymbol{\chi}(T)\cdot\delta\boldsymbol{\omega}(T) - \boldsymbol{\chi}(0)\cdot\delta\boldsymbol{\omega}(0) - \int_0^T \frac{1}{J}\left[\frac{\mathrm{d}\boldsymbol{T}_a}{\mathrm{d}\boldsymbol{\omega}}\right]^*\boldsymbol{\chi}\cdot\delta\boldsymbol{\omega}\,\mathrm{d}t \\
&\quad + \int_0^T\int_\Omega\left(\sum_{i,j}\int_0^1 G(\boldsymbol{x}-\boldsymbol{x}^{ij}(\mu))\left(\frac{\mathrm{d}\boldsymbol{F}^{ij}}{\mathrm{d}\omega^i}\delta\omega^i\right)\mathrm{d}\mu\right)\cdot\boldsymbol{\xi}\,\mathrm{d}\boldsymbol{x}\mathrm{d}t \\
&= \int_0^T -(\mathbb{T}+\boldsymbol{\Upsilon})\cdot\delta\boldsymbol{\omega} - \frac{\mathrm{d}\boldsymbol{\chi}}{\mathrm{d}t}\cdot\delta\boldsymbol{\omega}\,\mathrm{d}t + \boldsymbol{\chi}(T)\cdot\delta\boldsymbol{\omega}(T) - \boldsymbol{\chi}(0)\cdot\delta\boldsymbol{\omega}(0) - \int_0^T \frac{1}{J}\left[\frac{\mathrm{d}\boldsymbol{T}_a}{\mathrm{d}\boldsymbol{\omega}}\right]^*\boldsymbol{\chi}\cdot\delta\boldsymbol{\omega}\,\mathrm{d}t \\
&\quad + \int_0^T\left(\sum_{i,j}\int_0^1 \frac{\mathrm{d}\boldsymbol{F}^{ij}}{\mathrm{d}\omega^i}\cdot\left(\int_\Omega G(\boldsymbol{x}-\boldsymbol{x}^{ij}(\mu))\boldsymbol{\xi}\,\mathrm{d}\boldsymbol{x}\right)\mathrm{d}\mu\right)\delta\omega^i\,\mathrm{d}t,
\end{aligned} \tag{A7}$$

where $\mathbb{T} = \boldsymbol{T}_g - 2\gamma_1\max[0,\boldsymbol{\omega}-\omega^{max}] + 2\gamma_2\max[0,\omega^{min}-\boldsymbol{\omega}]$. Consequently, the adjoint equation of rotation corresponds to

$$-\frac{\mathrm{d}\boldsymbol{\chi}}{\mathrm{d}t} - (\mathbb{T}+\boldsymbol{\Upsilon}) - \frac{1}{J}\left[\frac{\mathrm{d}\boldsymbol{T}_a}{\mathrm{d}\boldsymbol{\omega}}\right]^*\boldsymbol{\chi} + \sum_j \mathbf{1}_i\int_0^1 \frac{\mathrm{d}\boldsymbol{F}^{ij}}{\mathrm{d}\omega^i}\cdot\left(\int_\Omega G(\boldsymbol{x}-\boldsymbol{x}^{ij}(\mu))\boldsymbol{\xi}\,\mathrm{d}\boldsymbol{x}\right)\mathrm{d}\mu = 0, \tag{A8}$$

with terminal condition $\boldsymbol{\chi}(T) = 0$ [and since $\delta\boldsymbol{\omega}(0) = 0$]. Again, $\mathrm{d}\boldsymbol{T}_a/\mathrm{d}\boldsymbol{\omega}$ is diagonal so that $[\mathrm{d}\boldsymbol{T}_a/\mathrm{d}\boldsymbol{\omega}]^* = \mathrm{d}\boldsymbol{T}_a/\mathrm{d}\boldsymbol{\omega}$. Expressions for the Jacobians $= \mathrm{d}\boldsymbol{T}_a/\mathrm{d}\boldsymbol{\omega}$ and $\mathrm{d}\boldsymbol{F}^{ij}/\mathrm{d}\omega^i$ are provided in Appendix A 5.

3. Adjoint rotor-position equation

The adjoint rotor-position equation is obtained by casting $\mathscr{L}_{\boldsymbol{\theta}}(\delta\boldsymbol{\theta}) = 0$ in its Riesz representation form. Thus

$$\begin{aligned}
\mathscr{L}_{\boldsymbol{\theta}}(\delta\boldsymbol{\theta}) &= \int_0^T\int_\Omega -\left(\frac{\mathrm{d}\boldsymbol{f}}{\mathrm{d}\boldsymbol{\theta}}\delta\boldsymbol{\theta}\right)\cdot\boldsymbol{\xi}\,\mathrm{d}\boldsymbol{x}\mathrm{d}t + \int_0^T -\frac{1}{J}\left(\frac{\mathrm{d}\boldsymbol{T}_a}{\mathrm{d}\boldsymbol{\theta}}\delta\boldsymbol{\theta}\right)\cdot\boldsymbol{\chi}\,\mathrm{d}t + \int_0^T \frac{\mathrm{d}\delta\boldsymbol{\theta}}{\mathrm{d}t}\cdot\boldsymbol{\Upsilon}\,\mathrm{d}t, \\
&= \int_0^T\int_\Omega\left(\sum_{i,j}\int_0^1 G(\boldsymbol{x}-\boldsymbol{x}^{ij}(\mu))\left(\frac{\mathrm{d}\boldsymbol{F}^{ij}}{\mathrm{d}\theta^i}\delta\theta^i\right)\mathrm{d}\mu\right)\cdot\boldsymbol{\xi}\,\mathrm{d}\boldsymbol{x}\mathrm{d}t \\
&\quad + \int_0^T\int_\Omega\left(\sum_{i,j}\int_0^1\left(\frac{\mathrm{d}G(\boldsymbol{x}-\boldsymbol{x}^{ij}(\mu))}{\mathrm{d}\theta^i}\delta\theta^i\right)\boldsymbol{F}^{ij}\,\mathrm{d}\mu\right)\cdot\boldsymbol{\xi}\,\mathrm{d}\boldsymbol{x}\mathrm{d}t \\
&\quad - \int_0^T\frac{1}{J}\left[\frac{\mathrm{d}\boldsymbol{T}_a}{\mathrm{d}\boldsymbol{\theta}}\right]^*\boldsymbol{\chi}\cdot\delta\boldsymbol{\theta}\,\mathrm{d}t - \int_0^T\frac{\mathrm{d}\boldsymbol{\Upsilon}}{\mathrm{d}t}\cdot\delta\boldsymbol{\theta}\,\mathrm{d}t + \boldsymbol{\Upsilon}(T)\cdot\delta\boldsymbol{\theta}(T) - \boldsymbol{\Upsilon}(0)\cdot\delta\boldsymbol{\theta}(0), \\
&= \int_0^T\left(\sum_{i,j}\int_0^1\frac{\mathrm{d}\boldsymbol{F}^{ij}}{\mathrm{d}\theta^i}\cdot\left(\int_\Omega G(\boldsymbol{x}-\boldsymbol{x}^{ij}(\mu))\boldsymbol{\xi}\,\mathrm{d}\boldsymbol{x}\right)\mathrm{d}\mu\right)\delta\theta^i\,\mathrm{d}t \\
&\quad + \int_0^T\left(\sum_{i,j}\int_0^1\boldsymbol{F}^{ij}\cdot\left(\int_\Omega\frac{\mathrm{d}G(\boldsymbol{x}-\boldsymbol{x}^{ij}(\mu))}{\mathrm{d}\theta^i}\boldsymbol{\xi}\,\mathrm{d}\boldsymbol{x}\right)\mathrm{d}\mu\right)\delta\theta^i\,\mathrm{d}t \\
&\quad - \int_0^T\frac{1}{J}\left[\frac{\mathrm{d}\boldsymbol{T}_a}{\mathrm{d}\boldsymbol{\theta}}\right]^*\boldsymbol{\chi}\cdot\delta\boldsymbol{\theta}\,\mathrm{d}t - \int_0^T\frac{\mathrm{d}\boldsymbol{\Upsilon}}{\mathrm{d}t}\cdot\delta\boldsymbol{\theta}\,\mathrm{d}t + \boldsymbol{\Upsilon}(T)\cdot\delta\boldsymbol{\theta}(T) - \boldsymbol{\Upsilon}(0)\cdot\delta\boldsymbol{\theta}(0).
\end{aligned}$$

Furthermore, $\delta\boldsymbol{\theta}(0) = 0$, and $[\mathrm{d}\boldsymbol{T}_a/\mathrm{d}\boldsymbol{\theta}]^* = \mathrm{d}\boldsymbol{T}_a/\mathrm{d}\boldsymbol{\theta}$, so that the adjoint rotor-position equation is given by

$$-\frac{\mathrm{d}\boldsymbol{\Upsilon}}{\mathrm{d}t} - \frac{1}{J}\frac{\mathrm{d}\boldsymbol{T}_a}{\mathrm{d}\boldsymbol{\theta}}\boldsymbol{\chi} + \sum_{i,j}\int_0^1 \frac{\mathrm{d}\boldsymbol{F}^{ij}}{\mathrm{d}\theta^i}\cdot\left(\int_\Omega G(\boldsymbol{x}-\boldsymbol{x}^{ij}(\mu))\boldsymbol{\xi}\,\mathrm{d}\boldsymbol{x}\right)\mathrm{d}\mu + \sum_{i,j}\int_0^1 \boldsymbol{F}^{ij}\cdot\left(\int_\Omega \frac{\mathrm{d}G(\boldsymbol{x}-\boldsymbol{x}^{ij}(\mu))}{\mathrm{d}\theta^i}\boldsymbol{\xi}\,\mathrm{d}\boldsymbol{x}\right)\mathrm{d}\mu = 0, \quad \text{(A9)}$$

with terminal condition $\boldsymbol{\Upsilon}(T) = 0$. Expressions for the Jacobians are provided in Appendix A 5.

4. Adjoint ALM turbine forces

The adjoint turbine forces arise in the adjoint momentum equations that follow from $\mathscr{L}_{\widetilde{\boldsymbol{u}}}(\delta\widetilde{\boldsymbol{u}}) = 0$. Here, we do not derive the full momentum equations, but rather focus on all terms that arise from the differentiation of the actuator line model to $\widetilde{\boldsymbol{u}}$, defining the adjoint forces. We obtain

$$\begin{aligned}(\boldsymbol{f}^*,\delta\widetilde{\boldsymbol{u}}) &= \int_0^T\int_\Omega -\left(\frac{\mathrm{d}\boldsymbol{f}}{\mathrm{d}\widetilde{\boldsymbol{u}}}\delta\widetilde{\boldsymbol{u}}\right)\cdot\boldsymbol{\xi}\,\mathrm{d}\boldsymbol{x}\mathrm{d}t + \int_0^T -\frac{1}{J}\left(\frac{\mathrm{d}\boldsymbol{T}_a}{\mathrm{d}\widetilde{\boldsymbol{u}}}\delta\widetilde{\boldsymbol{u}}\right)\cdot\boldsymbol{\chi}\,\mathrm{d}t\\ &= \int_0^T\int_\Omega\left(\sum_{i,j}\int_0^1 G(\boldsymbol{x}-\boldsymbol{x}^{ij}(\theta^i,\mu))\left(\frac{\mathrm{d}\boldsymbol{F}^{ij}}{\mathrm{d}\boldsymbol{v}^{ij}}\frac{\mathrm{d}\boldsymbol{v}^{ij}}{\mathrm{d}\widetilde{\boldsymbol{u}}}\delta\widetilde{\boldsymbol{u}}\right)\mathrm{d}\mu\right)\cdot\boldsymbol{\xi}\,\mathrm{d}\boldsymbol{x}\mathrm{d}t\\ &\quad -\int_0^T\sum_{i,j}\frac{1}{J}\left(\int_0^1\frac{\mathrm{d}T_a^{ij}}{\mathrm{d}\boldsymbol{v}^{ij}}\frac{\mathrm{d}\boldsymbol{v}^{ij}}{\mathrm{d}\widetilde{\boldsymbol{u}}}\delta\widetilde{\boldsymbol{u}}\,\mathrm{d}\mu\right)\chi_i\,\mathrm{d}t.\end{aligned} \quad \text{(A10)}$$

Using

$$\frac{\mathrm{d}\boldsymbol{v}^{ij}}{\mathrm{d}\widetilde{\boldsymbol{u}}}\delta\widetilde{\boldsymbol{u}} = \int_\Omega H(\boldsymbol{x}-\boldsymbol{x}^{ij}(\theta^i,\mu))\delta\widetilde{\boldsymbol{u}}\,\mathrm{d}\boldsymbol{x}, \quad \text{(A11)}$$

this further leads to

$$\begin{aligned}(\boldsymbol{f}^*,\delta\widetilde{\boldsymbol{u}}) &= \int_0^T\int_\Omega\int_\Omega\left(\sum_{i,j}\int_0^1 G(\boldsymbol{x}-\boldsymbol{x}^{ij})H(\boldsymbol{x}'-\boldsymbol{x}^{ij})\left(\frac{\mathrm{d}\boldsymbol{F}^{ij}}{\mathrm{d}\boldsymbol{v}^{ij}}\delta\widetilde{\boldsymbol{u}}\right)\mathrm{d}\mu\right)\cdot\boldsymbol{\xi}\,\mathrm{d}\boldsymbol{x}'\,\mathrm{d}\boldsymbol{x}\mathrm{d}t\\ &\quad -\int_0^T\int_\Omega\sum_{i,j}\frac{1}{J}\left(\int_0^1\frac{\mathrm{d}T_a^{ij}}{\mathrm{d}\boldsymbol{v}^{ij}}H(\boldsymbol{x}-\boldsymbol{x}^{ij})\delta\widetilde{\boldsymbol{u}}\,\mathrm{d}\mu\right)\chi_i\,\mathrm{d}\boldsymbol{x}\,\mathrm{d}t\\ &= \int_0^T\int_\Omega\left(\sum_{i,j}\int_0^1 H(\boldsymbol{x}'-\boldsymbol{x}^{ij})\left(\frac{\mathrm{d}\boldsymbol{F}^{ij}}{\mathrm{d}\boldsymbol{v}^{ij}}\right)^T\left[\int_\Omega G(\boldsymbol{x}-\boldsymbol{x}^{ij})\boldsymbol{\xi}\,\mathrm{d}\boldsymbol{x}\right]\mathrm{d}\mu\right)\cdot\delta\widetilde{\boldsymbol{u}}\,\mathrm{d}\boldsymbol{x}'\mathrm{d}t\\ &\quad -\int_0^T\int_\Omega\sum_{i,j}\left(\int_0^1 H(\boldsymbol{x}-\boldsymbol{x}^{ij})\frac{1}{J}\frac{\mathrm{d}T_a^{ij}}{\mathrm{d}\boldsymbol{v}^{ij}}\chi_i\,\mathrm{d}\mu\right)\cdot\delta\widetilde{\boldsymbol{u}}\,\mathrm{d}\boldsymbol{x}\,\mathrm{d}t.\end{aligned} \quad \text{(A12)}$$

Thus,

$$\boldsymbol{f}^* = \sum_{i,j}\int_0^1 H(\boldsymbol{x}-\boldsymbol{x}^{ij})\left\{\left(\frac{\mathrm{d}\boldsymbol{F}^{ij}}{\mathrm{d}\boldsymbol{v}^{ij}}\right)^T\left[\int_\Omega G(\boldsymbol{x}-\boldsymbol{x}^{ij})\boldsymbol{\xi}\,\mathrm{d}\boldsymbol{x}\right] - \frac{1}{J}\frac{\mathrm{d}T_a^{ij}}{\mathrm{d}\boldsymbol{v}^{ij}}\chi_i\right\}\mathrm{d}\mu. \quad \text{(A13)}$$

Expressions for $\mathrm{d}\boldsymbol{F}^{ij}/\mathrm{d}\boldsymbol{v}^{ij}$ and $\mathrm{d}T_a^{ij}/\mathrm{d}\boldsymbol{v}^{ij}$ are further provided in Appendix A 5.

5. Jacobian expressions

Expressions for derivatives to $\boldsymbol{\beta}$, ψ^{ij}, $\boldsymbol{\omega}$, $\boldsymbol{\theta}$, and $\boldsymbol{v}^{ij}$ are assembled in Appendixes A 5 a–A 5 e.

a. Derivatives to $\boldsymbol{\beta}$

First of all, $(\mathrm{d}\boldsymbol{T}_a/\mathrm{d}\boldsymbol{\beta})\boldsymbol{\chi} = \sum_i \mathrm{d}T_a^i/\mathrm{d}\beta^i\,\chi_i$, with

$$\frac{\mathrm{d}T_a^i}{\mathrm{d}\beta^i} = -\int_0^1\sum_{j=1}^{N_b} q^{ij}\left(\frac{\mathrm{d}C_l}{\mathrm{d}\alpha}\sin\psi^{ij} - \frac{\mathrm{d}C_d}{\mathrm{d}\alpha}\cos\psi^{ij}\right)c(\mu)R\,\mu\,\mathrm{d}\mu. \quad \text{(A14)}$$

Second,

$$\begin{aligned}\frac{\mathrm{d}F_1^{ij}}{\mathrm{d}\beta^i} &= -q^{ij}\left(\frac{\mathrm{d}C_l}{\mathrm{d}\alpha}\cos\psi^{ij} + \frac{\mathrm{d}C_d}{\mathrm{d}\alpha}\sin\psi^{ij}\right)c(\mu),\\ \frac{\mathrm{d}F_2^{ij}}{\mathrm{d}\beta^i} &= +q^{ij}\left(\frac{\mathrm{d}C_l}{\mathrm{d}\alpha}\sin\psi^{ij} - \frac{\mathrm{d}C_d}{\mathrm{d}\alpha}\cos\psi^{ij}\right)c(\mu)\sin(\theta^i+\Delta\theta^j),\\ \frac{\mathrm{d}F_3^{ij}}{\mathrm{d}\beta^i} &= -q^{ij}\left(\frac{\mathrm{d}C_l}{\mathrm{d}\alpha}\sin\psi^{ij} - \frac{\mathrm{d}C_d}{\mathrm{d}\alpha}\cos\psi^{ij}\right)c(\mu)\cos(\theta^i+\Delta\theta^j),\end{aligned} \quad \text{(A15)}$$

where the derivatives $\mathrm{d}C_l/\mathrm{d}\alpha$ and $\mathrm{d}C_d/\mathrm{d}\alpha$ are evaluated at every blade ij individually, by employing a first order forward difference scheme on the tabulated lift and drag tables from Ref. 30.

b. Derivatives to ψ^{ij}

We have

$$\frac{\mathrm{d}T_a^{ij}}{\mathrm{d}\psi^{ij}} = q^{ij}c(\mu)R\mu\left(C_l\cos\psi^{ij} + C_d\sin\psi^{ij} + \frac{\mathrm{d}C_l}{\mathrm{d}\alpha}\sin\psi^{ij} - \frac{\mathrm{d}C_d}{\mathrm{d}\alpha}\cos\psi^{ij}\right), \tag{A16}$$

and

$$\begin{aligned}
\frac{\mathrm{d}F_1^{ij}}{\mathrm{d}\psi^{ij}} &= q^{ij}c(\mu)\left(-C_l\sin\psi^{ij} + C_d\cos\psi^{ij} + \frac{\mathrm{d}C_l}{\mathrm{d}\alpha}\cos\psi^{ij} + \frac{\mathrm{d}C_d}{\mathrm{d}\alpha}\sin\psi^{ij}\right),\\
\frac{\mathrm{d}F_2^{ij}}{\mathrm{d}\psi^{ij}} &= -q^{ij}c(\mu)\left(C_l\cos\psi^{ij} + C_d\sin\psi^{ij} + \frac{\mathrm{d}C_l}{\mathrm{d}\alpha}\sin\psi^{ij} - \frac{\mathrm{d}C_d}{\mathrm{d}\alpha}\cos\psi^{ij}\right)\sin(\theta^i + \Delta\theta^j),\\
\frac{\mathrm{d}F_3^{ij}}{\mathrm{d}\psi^{ij}} &= q^{ij}c(\mu)\left(C_l\cos\psi^{ij} + C_d\sin\psi^{ij} + \frac{\mathrm{d}C_l}{\mathrm{d}\alpha}\sin\psi^{ij} - \frac{\mathrm{d}C_d}{\mathrm{d}\alpha}\cos\psi^{ij}\right)\cos(\theta^i + \Delta\theta^j).
\end{aligned} \tag{A17}$$

As discussed above (see Appendix A 1), the derivatives $\mathrm{d}C_l/\mathrm{d}\alpha$ and $\mathrm{d}C_d/\mathrm{d}\alpha$ are evaluated using interpolations of tabulated data.

c. Derivatives to ω

First, $(\mathrm{d}\boldsymbol{T}_a/\mathrm{d}\boldsymbol{\omega})\boldsymbol{\chi} = \sum_i \mathrm{d}T_a^i/\mathrm{d}\omega^i\,\chi_i$, with

$$\begin{aligned}
\frac{\mathrm{d}T_a^i}{\mathrm{d}\omega^i} = \int_0^1 \sum_{j=1}^{N_b}\Big[&(\omega_i R\mu - v_\theta^{ij})\left(C_l\sin\psi^{ij} - C_d\cos\psi^{ij}\right)\\
&\times c(\mu)(R\mu)^2 + \frac{\mathrm{d}T_a^{ij}}{\mathrm{d}\psi^{ij}}\frac{\mathrm{d}\psi^{ij}}{\mathrm{d}\omega^i}\Big]\,\mathrm{d}\mu,
\end{aligned} \tag{A18}$$

with $\partial T_a^{ij}/\partial\psi^{ij}$ given by Eq. (A16), and

$$\frac{\mathrm{d}\psi^{ij}}{\mathrm{d}\omega_i} = -\frac{v_1^{ij}R\mu}{(v_1^{ij})^2 + (\omega_i R\mu - v_\theta^{ij})^2}. \tag{A19}$$

Second, the first element of $\mathrm{d}\boldsymbol{F}^{ij}/\mathrm{d}\omega^i$ is given by

$$\begin{aligned}
\frac{\mathrm{d}F_1^{ij}}{\mathrm{d}\omega^i} = {}& R\mu(\omega_i R\mu - v_\theta^{ij})\left(C_l\cos\psi^{ij} + C_d\sin\psi^{ij}\right)c(\mu)\\
&+ \frac{\partial F_1^{ij}}{\partial\psi^{ij}}\frac{\mathrm{d}\psi^{ij}}{\mathrm{d}\omega_i},
\end{aligned} \tag{A20}$$

and similar expressions are straightforwardly obtained for $\mathrm{d}F_2^{ij}/\mathrm{d}\omega^i$ and $\mathrm{d}F_3^{ij}/\mathrm{d}\omega^i$.

d. Derivatives to θ

First of all, $\mathrm{d}T_a^i/\mathrm{d}\theta^i = \int_0^1 \sum_{j=1}^{N_b}\mathrm{d}T_a^{ij}/\mathrm{d}\theta^i\,\mathrm{d}\mu$, where

$$\frac{\mathrm{d}T_a^{ij}}{\mathrm{d}\theta^i} = \frac{\mathrm{d}T_a^{ij}}{\mathrm{d}\boldsymbol{v}^{ij}}\frac{\mathrm{d}\boldsymbol{v}^{ij}}{\mathrm{d}\theta^i}. \tag{A21}$$

Similarly,

$$\frac{\mathrm{d}\boldsymbol{F}^{ij}}{\mathrm{d}\theta^i} = \frac{\partial\boldsymbol{F}^{ij}}{\partial\theta^i} + \frac{\mathrm{d}\boldsymbol{F}^{ij}}{\mathrm{d}\boldsymbol{v}^{ij}}\frac{\mathrm{d}\boldsymbol{v}^{ij}}{\mathrm{d}\theta^i}. \tag{A22}$$

Expressions for $\mathrm{d}\boldsymbol{F}^{ij}/\mathrm{d}\boldsymbol{v}^{ij}$ and $\mathrm{d}T_a^{ij}/\mathrm{d}\boldsymbol{v}^{ij}$ are provided in Appendix A 5 e. Moreover, it is readily seen that $\frac{\partial\boldsymbol{F}^{ij}}{\partial\theta^i} = [0, -\cos(\theta^i + \Delta\theta^j), -\sin(\theta^i + \Delta\theta^j)]q^{ij}(C_l\sin\psi^{ij} - C_d\cos\psi^{ij})c(\mu)$. Furthermore,

$$\frac{\mathrm{d}\boldsymbol{v}^{ij}}{\mathrm{d}\theta^i} = \int_\Omega \frac{\mathrm{d}}{\mathrm{d}\theta^i}\left[\prod_{k=1}^{3} H_k(x_k - x_k^{ij}(\theta^i,\mu))\right]\widetilde{\boldsymbol{u}}(\boldsymbol{x},t)\,\mathrm{d}\boldsymbol{x}, \tag{A23}$$

where

$$\frac{\mathrm{d}H_k(x_k - x_k^{ij})}{\mathrm{d}\theta^i} = \begin{cases}\dfrac{1}{\Delta_k}\mathrm{sign}(x_k - x_k^{ij})\dfrac{\mathrm{d}x_k^{ij}}{\mathrm{d}\theta^i} & \text{for } |x_k - x_k^{ij}(\theta^i,\mu)| < \Delta_k\\ 0 & \text{otherwise,}\end{cases} \tag{A24}$$

with $\mathrm{d}\boldsymbol{x}^{ij}/\mathrm{d}\theta^i = [0, -R\mu\sin(\theta^i + \Delta\theta^j), R\mu\cos(\theta^i + \Delta\theta^j)]$.

Finally,

$$\begin{aligned}
\frac{\mathrm{d}G(\boldsymbol{x} - \boldsymbol{x}^{ij})}{\mathrm{d}\theta^i} = {}& G(\boldsymbol{x} - \boldsymbol{x}^{ij})12z\left(\frac{-(x_2 - x_2^{ij})\sin(\theta^i + \Delta\theta^j)}{\epsilon_2^2}\right.\\
&\left.+ \frac{(x_3 - x_3^{ij})\cos(\theta^i + \Delta\theta^j)}{\epsilon_3^2}\right),
\end{aligned} \tag{A25}$$

with $z = (\sum_{k=1}^{3}[(x_k - x_k^{ij})/\epsilon_k]^2)^{1/2}$.

e. Derivatives to v^{ij}

Applying the chain rule, we find

$$\frac{\mathrm{d}T_a^{ij}}{\mathrm{d}\boldsymbol{v}^{ij}} = \frac{\partial T_a^{ij}}{\partial\boldsymbol{v}^{ij}} + \frac{\partial T_a^{ij}}{\partial\psi^{ij}}\frac{\mathrm{d}\psi^{ij}}{\mathrm{d}\boldsymbol{v}^{ij}}, \tag{A26}$$

$$\frac{\mathrm{d}\boldsymbol{F}^{ij}}{\mathrm{d}\boldsymbol{v}^{ij}} = \frac{\partial\boldsymbol{F}^{ij}}{\partial\boldsymbol{v}^{ij}} + \frac{\partial\boldsymbol{F}^{ij}}{\partial\psi^{ij}}\frac{\mathrm{d}\psi^{ij}}{\mathrm{d}\boldsymbol{v}^{ij}}. \tag{A27}$$

Expressions for $\partial T_a^{ij}/\partial\psi^{ij}$ and $\partial\boldsymbol{F}^{ij}/\partial\psi^{ij}$ are given in Appendix A 5 b. Further elaborations of $\mathrm{d}\psi^{ij}/\mathrm{d}\boldsymbol{v}^{ij}$, $\partial T_a^{ij}/\partial\boldsymbol{v}^{ij}$, and $\partial\boldsymbol{F}^{ij}/\partial\boldsymbol{v}^{ij}$, are straightforward, but omitted here for brevity.

APPENDIX B: DISCRETE ADJOINT RUNGE–KUTTA TIME INTEGRATION

Remark that the explicit Runge–Kutta method is not self-adjoint so that the discrete adjoint formulation differs slightly from the forward formulation. Details can be, e.g., found in Refs. 41 and 42. The forward Runge–Kutta method corresponds to[43]

$$\boldsymbol{q}_i^n = \boldsymbol{q}^n + \Delta t\sum_{j=1}^{4} a_{ij}R(\boldsymbol{q}_j^n, \boldsymbol{\varphi}_j^n), \tag{B1}$$

$$\boldsymbol{q}^{n+1} = \boldsymbol{q}^n + \Delta t\sum_{i=1}^{4} b_i R(\boldsymbol{q}_i^n, \boldsymbol{\varphi}_i^n), \tag{B2}$$

with the classical RK4 coefficients

$$\boldsymbol{a} = \begin{bmatrix} 0 & 0 & 0 & 0 \\ \frac{1}{2} & 0 & 0 & 0 \\ 0 & \frac{1}{2} & 0 & 0 \\ 0 & 0 & 1 & 0 \end{bmatrix}, \boldsymbol{b} = \begin{bmatrix} \frac{1}{6} \\ \frac{2}{6} \\ \frac{2}{6} \\ \frac{1}{6} \end{bmatrix}.$$

Furthermore $\boldsymbol{q}^n$ and $\boldsymbol{q}^{n+1}$ are the forward states discretized at time step n and $n+1$, respectively, and $\boldsymbol{q}_i^n$ is the solution at the ith intermediate Runge–Kutta stage of nth time step. The adjoint Runge-Kutta method can then be derived to be[41,42]

$$\begin{aligned} \boldsymbol{q}^{*^n} &= \boldsymbol{q}^{*^{n+1}} + \sum_{j=1}^{4} \boldsymbol{q}_j^{*^n} - D_{\boldsymbol{q}}(\boldsymbol{q}^n, \boldsymbol{\varphi}^n), \\ \boldsymbol{q}_i^{*^n} &= \Delta t\, R_{\boldsymbol{q}}^*(\boldsymbol{q}_i^n, \boldsymbol{\varphi}_i^n)\left(b_i \boldsymbol{q}^{*^{n+1}} + \sum_{j=1}^{4} a_{ji} \boldsymbol{q}_j^{*^n}\right). \end{aligned} \tag{B3}$$

Above $\boldsymbol{q}^*$ and $R_{\boldsymbol{q}}^*$ are the adjoint states and the adjoint Jacobian, respectively. Furthermore, $D_{\boldsymbol{q}}$ denotes the partial derivative of the integrand of the cost functional with respect to the state variables.

APPENDIX C: GRADIENT VERIFICATION

In this appendix, we verify the implemented adjoint method by comparing the resulting gradient vector against the one computed with a finite difference method, for a limited set of control perturbations. The simulations are performed under uniform inflow conditions, using the computational setup described in Fig. 3. First an initialization simulation is performed by controlling both rotors with the MPPT algorithm until the wakes are fully developed. Next, a control window of 200 s with a MPPT controller is considered as the background state around which control sensitivity is investigated.

The adjoint-based sensitivity provides the gradient vector for every instance in time over the full 200 s control horizon at the cost of one simulation. Finite Differences (FDs) are much more expensive and require one simulation per control direction (i.e., generator torque and pitch sensitivity times number of time instances). Here, we evaluate the finite difference sensitivity for different time instances (for generator torque, $t = 0, 6, 10, 20, 26, 34, 49, 98, 147, 199$ s, and for blade pitch, $t = 0, 5, 10, 20, 28, 30, 36, 42, 49, 98, 199$ s), requiring 21 simulations in total for different perturbations $\delta\boldsymbol{\varphi}_i$ ($i = 1, \ldots, 21$), with $\|\delta\boldsymbol{\varphi}_i\| = 1$. The FD sensitivity is then evaluated using

$$\left(\nabla\tilde{\mathscr{J}}_i, \delta\boldsymbol{\varphi}_i\right) = \frac{\tilde{\mathscr{J}}(\boldsymbol{\varphi}_{\mathrm{MPPT}} + \alpha\delta\boldsymbol{\varphi}_i) - \tilde{\mathscr{J}}(\boldsymbol{\varphi}_{\mathrm{MPPT}})}{\alpha} + \mathcal{O}(\alpha^2). \tag{C1}$$

The step-size α is ideally selected such that $\|\Delta\tilde{\mathscr{J}}\|/\|\tilde{\mathscr{J}}\| \approx \epsilon_{\mathrm{machine}}^{1/2}$ as a rough trade-off between errors arising from arithmetic precision and higher order terms (see Ref. 40 for a discussion). Here, we find $\alpha \approx 10^{-4}$ to work well.

The adjoint and the finite difference gradient vectors are compared in Fig. 18, showing that agreement is very good. As far as the gradient of the cost functional with respect to the generator torque is considered, the relative error between the adjoint and the finite difference methods is found to be 7% (based on the L_2 norm of the gradient for all FD time instances), while it corresponds to 10% for the blade pitch gradient. It is further noticed that the adjoint pitch gradient shows some high-frequency oscillations. These are the numerical features of the ALM, but do not dominantly influence our optimization results (see discussion in the main text). The improvement of the gradient based on different interpolation and filtering strategies or the use of Sobolev smoothing is a subject of future research.

Looking at Fig. 18, it is also observed that the adjoint gradient error grows in the inverse time direction, in line with the general magnitude of the gradient. This is natural due to the fact that turbulence is a chaotic system so that any linear sensitivity evaluation (be it forward or backward) is bound to diverge.[20–22] This limits in practice the length of our optimal control window, which we take here to be 200 s.

Finally, we notice in Fig. 18 that gradient activity is mainly located in the the initial $T/3$ s of the time horizon. This is related to the fact that after the initial $T/3$ s, fluid particles do not have enough time to travel the distance between the rotors of the two turbines so that control actions have no impact on the second turbine anymore. This is a clear finite-time horizon effect of our receding-horizon approach. In order to minimize the impact on optimization results, we therefore select $T_A = T/3$.

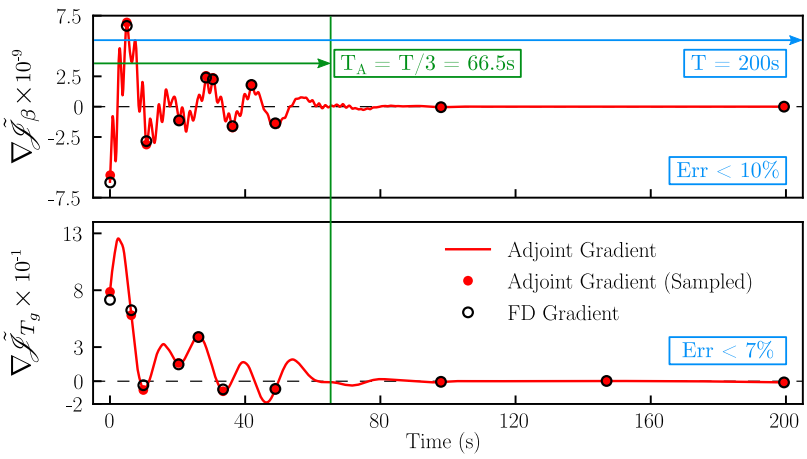

FIG. 18. Comparison of the adjoint and the finite difference gradients.

[1] J.-A. Dahlberg, "Assessment of the Lillgrund wind farm: Power performance wake effects," Vattenfall Vindkraft AB, 6_1 LG Pilot Report, http://www.vattenfall.se/sv/file/15_Assessment_of_the_Lillgrund_W.pdf_16596737.pdf (cited March 30, 2012), 2009.

[2] R. J. Barthelmie, S. C. Pryor, S. T. Frandsen, K. S. Hansen, J. G. Schepers, K. Rados, W. Schlez, A. Neubert, L. E. Jensen, and S. Neckelmann, "Quantifying the impact of wind turbine wakes on power output at offshore wind farms," J. Atmos. Oceanic Tech. **27**(8), 1302–1317 (2010).

[3] N. G. Nygaard, "Wakes in very large wind farms and the effect of neighbouring wind farms," J. Phys.: Conf. Ser. **524**, 012162 (2014).

[4] F. Porté-Agel, Y.-T. Wu, and C.-H. Chen, "A numerical study of the effects of wind direction on turbine wakes and power losses in a large wind farm," Energies **6**(10), 5297–5313 (2013).

[5] R. J. A. M. Stevens, D. F. Gayme, and C. Meneveau, "Large eddy simulation studies of the effects of alignment and wind farm length," J. Renewable Sustainable Energy **6**(2), 023105 (2014).

[6] R. J. A. M. Stevens, "Dependence of optimal wind turbine spacing on wind farm length," Wind Energy **19**(4), 651–663 (2016).

[7] R. J. A. M. Stevens, D. F. Gayme, and C. Meneveau, "Effects of turbine spacing on the power output of extended wind-farms," Wind Energy **19**(2), 359–370 (2016).

[8] J. Meyers and C. Meneveau, "Optimal turbine spacing in fully developed wind farm boundary layers," Wind Energy **15**(2), 305–317 (2012).

[9] M. Steinbuch, W. W. de Boer, O. H. Bosgra, S. A. W. M. Peters, and J. Ploeg, "Optimal control of wind power plants," J. Wind Eng. Ind. Aerodyn. **27**(1), 237–246 (1988).

[10] J. Annoni, P. M. O. Gebraad, A. K. Scholbrock, P. A. Fleming, and J.-W. van Wingerden, "Analysis of axial-induction-based wind plant control using an engineering and a high-order wind plant model," Wind Energy **19**(6), 1135–1150 (2016).

[11] J. Bartl and L. Sætran, "Blind test comparison of the performance and wake flow between two in-line wind turbines exposed to different turbulent inflow conditions," Wind Energy Sci. **2**(1), 55–76 (2017).

[12] P. M. O. Gebraad, P. A. Fleming, and J.-W. van Wingerden, "Comparison of actuation methods for wake control in wind plants," in *American Control Conference (ACC), 2015* (IEEE, 2015), pp. 1695–1701.

[13] M. J. Churchfield, P. Fleming, B. Bulder, S. M. White *et al.*, "Wind turbine wake-redirection control at the Fishermen's Atlantic City Windfarm," in *Offshore Technology Conference* (Offshore Technology Conference, 2015).

[14] F. Campagnolo, V. Petrović, C. L. Bottasso, and A. Croce, "Wind tunnel testing of wake control strategies," in *American Control Conference (ACC), 2016* (IEEE, 2016), pp. 513–518.

[15] J. P. Goit and J. Meyers, "Optimal control of energy extraction in wind-farm boundary layers," J. Fluid Mech. **768**, 5–50 (2015).

[16] J. P. Goit, W. Munters, and J. Meyers, "Optimal coordinated control of power extraction in LES of a wind farm with entrance effects," Energies **9**(1), 29 (2016).

[17] W. Munters and J. Meyers, "An optimal control framework for dynamic induction control of wind farms and their interaction with the atmospheric boundary layer," Philos. Trans. R. Soc., A **375**(2091), 20160100 (2017).

[18] W. Munters and J. Meyers, "Optimal coordinated control of wind-farm boundary layers in large-eddy simulations: Intercomparison between dynamic yaw control and dynamic induction control," Energies **11**, 177 (2018).

[19] W. Munters and J. Meyers, "Towards practical dynamic induction control of wind farms: Analysis of optimally controlled wind-farm boundary layers and sinusoidal induction control of first-row turbines," Wind Energy Sci. **3**, 409–425 (2018).

[20] P. Blonigan, S. Gomez, and Q. Wang, "Least squares shadowing for sensitivity analysis of turbulent fluid flows," AIAA Paper No. 2014-1426, 2014.

[21] P. J. Blonigan and Q. Wang, "Multiple shooting shadowing for sensitivity analysis of chaotic dynamical systems," J. Comput. Phys. **354**, 447–475 (2018).

[22] M. Chater, A. Ni, and Q. Wang, "Simplified least squares shadowing sensitivity analysis for chaotic ODEs and PDEs," J. Comput. Phys. **329**, 126–140 (2017).

[23] T. R. Bewley, P. Moin, and R. Temam, "DNS-based predictive control of turbulence: An optimal benchmark for feedback algorithms," J. Fluid Mech. **447**, 179–225 (2001).

[24] J. Meyers and C. Meneveau, "Large eddy simulations of large wind-turbine arrays in the atmospheric boundary layer," AIAA 2010-827, 2010.

[25] J. Meyers and P. Sagaut, "On the model coefficients for the standard and the variational multi-scale Smagorinsky model," J. Fluid Mech. **569**, 287–319 (2006).

[26] J. Meyers, "Error-landscape assessment of large-eddy simulations: A review of the methodology," J. Sci. Comput. **49**(1), 65–77 (2011).

[27] J. N. Sorensen and W. Z. Shen, "Numerical modeling of wind turbine wakes," J. Fluids Eng. **124**(2), 393–399 (2002).

[28] J. F. Manwell, J. G. McGowan, and A. L. Rogers, *Wind Energy Explained: Theory, Design and Application* (John Wiley & Sons, 2010).

[29] L. Y. Pao and K. E. Johnson, "A tutorial on the dynamics and control of wind turbines and wind farms," in *Proceedings of the 2009 Conference on American Control Conference, ACC'09* (IEEE Press, Piscataway, NJ, United States, 2009), pp. 2076–2089, ISBN: 978-1-4244-4523-3, URL http://dl.acm.org/citation.cfm?id=1702315.1702657.

[30] J. Jonkman, S. Butterfield, W. Musial, and G. Scott, "Definition of a 5-mw reference wind turbine for offshore system development," Technical Report No. NREL/TP-500-38060, National Renewable Energy Laboratory (NREL), Golden, CO, 2009.

[31] L. A. Martínez-Tossas, M. J. Churchfield, and S. Leonardi, "Large eddy simulations of the flow past wind turbines: Actuator line and disk modeling," Wind Energy **18**(6), 1047–1060 (2015).

[32] L. A. Martnez-Tossas, M. J. Churchfield, and C. Meneveau, "Optimal smoothing length scale for actuator line models of wind turbine blades based on Gaussian body force distribution," Wind Energy **20**(6), 1083–1096 (2017).

[33] A. Borzì and V. Schulz, *Computational Optimization of Systems Governed by Partial Differential Equations* (SIAM, 2011).

[34] R. H. Byrd, P. Lu, J. Nocedal, and C. Zhu, "A limited memory algorithm for bound constrained optimization," SIAM J. Sci. Comput. **16**(5), 1190–1208 (1995).

[35] J. Meyers and P. Sagaut, "Evaluation of Smagorinsky variants in large-eddy simulations of wall-resolved plane channel flows," Phys. Fluids **19**(9), 095105 (2007).

[36] S. Delport, M. Baelmans, and J. Meyers, "Constrained optimization of turbulent mixing-layer evolution," J. Turbul. **10**, N18 (2009).

[37] C. G. Canuto, M. Y. Hussaini, A. Quarteroni, and T. A. Zang, *Spectral Methods: Fundamentals in Single Domains* (Springer, 2010).

[38] R. W. C. P. Verstappen and A. E. P. Veldman, "Symmetry-preserving discretization of turbulent flow," J. Comput. Phys. **187**(1), 343–368 (2003).

[39] W. Munters, C. Meneveau, and J. Meyers, "Turbulent inflow precursor method with time-varying direction for large-eddy simulations and applications to wind farms," Boundary-Layer Meteorol. **159**(2), 305–328 (2016).

[40] C. Nita, S. Vandewalle, and J. Meyers, "On the efficiency of gradient based optimization algorithms for DNS-based optimal control in a turbulent channel flow," Comput. Fluids **125**, 11–24 (2016).

[41] W. W. Hager, "Runge-Kutta methods in optimal control and the transformed adjoint system," Numerische Math. **87**(2), 247–282 (2000).

[42] J. M. Sanz-Serna, "Symplectic Runge–Kutta schemes for adjoint equations, automatic differentiation, optimal control, and more," SIAM Rev. **58**(1), 3–33 (2016).

[43] E. Hairer and G. Wanner, *Solving Ordinary Differential Equations I*, Springer Series in Computational Mathematics (Springer Berlin Heidelberg, Berlin, Heidelberg, 1993), Vol. 8.

[44] P. K. Jha, M. J. Churchfield, P. J. Moriarty, and S. Schmitz, "Guidelines for volume force distributions within actuator line modeling of wind turbines on large-eddy simulation-type grids," J. Solar Energy Eng. **136**(3), 031003 (2014).

[45] P. R. Spalart, "Direct numerical study of leading-edge contamination," in *Fluid Dynamics of Three-Dimensional Turbulent Shear Flows and Transition* (AGARD, 1989), p. 5–1.

[46] J. Mann, "Wind field simulation," Probab. Eng. Mech. **13**(4), 269–282 (1998).

[47] L. Gilling, *TuGen: Synthetic Turbulence Generator, Manual and User's Guide*, DCE Technical Reports No. 76, Aalborg University, Department of Civil Engineering, 2009.

[48] L. E. M. Lignarolo, D. Ragni, C. Krishnaswami, Q. Chen, C. J. Simão Ferreira, and G. J. W. van Bussel, "Experimental analysis of the wake of a horizontal-axis wind-turbine model," Renewable Energy **70**, 31–46 (2014), special issue on aerodynamics of offshore wind energy systems and wakes.

[49] L. E. M. Lignarolo, D. Ragni, F. Scarano, C. J. Simão Ferreira, and G. J. W. van Bussel, "Tip-vortex instability and turbulent mixing in wind-turbine wakes," J. Fluid Mech. **781**, 467–493 (2015).

[50]J. N. Sørensen, R. F. Mikkelsen, D. S. Henningson, S. Ivanell, S. Sarmast, and S. J. Andersen, "Simulation of wind turbine wakes using the actuator line technique," Philos. Trans. R. Soc., A **373**(2035), 20140071 (2015).
[51]L. E. M. Lignarolo, D. Mehta, R. J. A. M. Stevens, A. E. Yilmaz, G. van Kuik, S. J. Andersen, C. Meneveau, C. J. Ferreira, D. Ragni, J. Meyers, G. J. W. van Bussel, and J. Holierhoek, "Validation of four LES and a vortex model against stereo-PIV measurements in the near wake of an actuator disc and a wind turbine," Renewable Energy **94**, 510–523 (2016).
[52]L. Martinez-Tossas, M. Churchfield, A. E. Yılmaz, H. Sarlak, P. Johnson, J. Sorensen, J. Meyers, and C. Meneveau, "Comparison of four large-eddy simulation research codes and effects of model coefficient and inflow turbulence in actuator line based wind turbine modeling," J. Renewable Sustainable Energy **10**, 033301 (2018).
[53]J. Neuberger, *Sobolev Gradients and Differential Equations* (Springer Science & Business Media, 2009).
[54]J. C. R. Hunt, A. A. Wray, and P. Moin, "Eddies, streams, and convergence zones in turbulent flows," in *Studying Turbulence Using Numerical Simulation Databases—II: Proceedings of the 1988 Summer Program* (Center for Turbulence Research, Stanford University, 1988), pp. 193–208, Report CTR-S88.
[55]S. Quallen and T. Xing, "CFD simulation of a floating offshore wind turbine system using a variable-speed generator-torque controller," Renewable Energy **97**, 230–242 (2016).
[56]K. Shariff and A. Leonard, "Vortex rings," Annu. Rev. Fluid Mech. **24**(1), 235–279 (1992).
[57]J.-Z. Wu, H.-Y. Ma, and M.-D. Zhou, *Vorticity and Vortex Dynamics* (Springer Science & Business Media, 2007).
[58]M. Van Dyke and M. Van Dyke, *An Album of Fluid Motion* (Parabolic Press Stanford, 1982).
[59]H. Choi, M. Hinze, and K. Kunisch, "Instantaneous control of backward-facing step flows," Appl. Numer. Math. **31**(2), 133–158 (1999).
[60]C. S. Peskin, "The immersed boundary method," Acta Numerica **11**, 479–517 (2002).
[61]X. Yang, F. Sotiropoulos, J. R. Conzemius, J. N. Wachtler, and M. B. Strong, "Large-eddy simulation of turbulent flow past wind turbines/farms: The virtual wind simulator (VWiS)," Wind Energy **18**(12), 2025–2045 (2015).
[62]X. Yang, X. Zhang, Z. Li, and G.-W. He, "A smoothing technique for discrete delta functions with application to immersed boundary method in moving boundary simulations," J. Comput. Phys. **228**(20), 7821–7836 (2009).